Direct numerical simulation of trapped-phase recirculation at low capillary number

Amir Hossein Mohammadi Alamooti, A H Mohammadi Alamooti, Qumars Azizi, Hossein Davarzani

Direct numerical simulation of trapped-phase recirculation at low capillary number

*A. H. Mohammadi Alamooti, Q. Azizi, H. Davarzani**

BRGM (French Geological Survey), 3 Avenue Claude Guillemin, Orléans, 45100, France

* Corresponding Author
Email: h.davarzani@brgm.fr. Phone: + 33 (0)2 38 64 33 52.

Abstract

Understanding multiphase flow in porous media, especially how velocity is distributed at the pore-scale, has been the aim of several studies. However, these studies address the recirculation behavior inside the trapped phase experimentally without any comprehensive numerical study of the impact of different governing mechanisms related to the fluid configurations and properties, including drag force and capillary number analysis at low capillary number regime. In this study, we analyzed the recirculation phenomenon inside the trapped phase for various displacement mechanisms, fluid configurations, and dynamic properties. To simulate the pore-scale displacement at low capillary number, we used a filtered surface-force formulation of volume of fluid method, which was implemented in a separately available solver for OpenFoam package. The results showed that within the ranges of capillary number of invading phase analyzed in this study (in the order of 1×10^{-7} to 1×10^{-2}), the recirculation phenomenon exists in trapped phases. During the imbibition mechanism, two stagnant regions are created adjacent to the fluid-fluid interface inside the invading fluid. Drag-force analysis on fluid-fluid interfaces shows that during imbibition the maximum force is exerted near the center of the interface, whereas during drainage more force is applied on two elongated interface tails on a solid surface. The centroids are elongated parallel to the interface during drainage and perpendicularly during imbibition, which is in concordance with drag-force distribution along

with the interface. The existence of a solid surface near the fluid-fluid interface affects the recirculation process in a way that one or more centroids can be created depending on displacement mechanisms. When the ratio of trapped-phase radius to cavity depth is lower, two simultaneous recirculation zones are formed inside the invading and trapped phases While the changes in viscosity ratio and interfacial tension shifted the centroid location inside the trapped zone, the center of rotation seems to be independent of injection velocity. The average velocity of trapped phase is individually a logarithmic function of the surface tension and fluids viscosity ratio. The stationariness of centroid results in a linear relationship between the average velocity inside the trapped zone and injection velocity. For all ranges of viscosity ratios, a linear relationship between the capillary number of invading and trapped phase is obtained. The findings of this study lead to a better understanding of trapping and mobilization mechanisms in microchannels where various forces are acting on fluid-fluid interfaces.

Keywords: Recirculation; volume of fluid; pore-doublet model; trapped phase, two-phase flow

Highlights

- Direct pore-scale modeling of two-phase flow by volume-of-fluid
- Recirculation in trapped phases for various fluid configurations in pore assembly
- More intensified recirculation for drainage mechanism to imbibition one
- Drag-force analysis on fluid-fluid/solid interfaces
- Role of fluid dynamic properties on recirculation processes

Nomenclature

List of symbols

Bo	Bond number (-)
Ca	Capillary number (-)
D	Drag force per unit of depth (N/m)
f	Force vector (N)
g	Gravity vector (m/s^2)
k	Interface curvature (1/m)
L	Characteristic length (m)
l	Length (m)
M	Viscosity ratio (-)
n	Unit normal (-)
P	Pressure (Pa)
t	Time (s)
U	Velocity (m/s)
x, y	Cartesian coordinate system (m)

Subscripts

ave	Average
b	Boundary
c	Capillary term
d	Dynamic
filt	Filter
i	Invading
inj	Injection
I	Interface
mag	Magnitude
nw	Non-wetting phase
s	Smooth
shp	Sharp
SSF	Sharp Surface Force
t	Trapping phase
w	Wetting phase
x, y	Co-ordinate plane

Greek symbols

α	Volume fraction of fluids (-)
δ	Dirac delta function (-)
μ	Viscosity (Pa. s)
ρ	Density (kg/m^3)
σ	Surface tension (N/m)

Coefficients and constants

C_{filt}	Capillary force filter
C_{shp}	Sharp VOF's color function
$C_{\delta t}$	FSF time step constant

1. Introduction

Transport phenomena at pore-scale have gained great prominence in recent years since they are of significant importance in a variety of areas including enhanced oil recovery (Zhao et al., 2010), soil remediation (Aminnaji et al., 2019), and carbon/hydrogen storage (Ebigbo et al., 2013; Riazi et al., 2011). Various microscale forces including capillary, viscous, inertial, and gravitational forces play an important role in fluid dynamics especially at the interface (Dejam et al., 2014; Ferrari and Lunati, 2014, 2013; Mashayekhizadeh et al., 2011; Méheust et al., 2002; Raeini et al., 2014). The roles of rock and fluid properties that can significantly affect the displacement process are also important (Avraam and Payatakes, 1995).

Specifically, pore-scale investigation is a strong tool that can shed light on the subsurface process at the microscale. To investigate the physics of fluid flow at pore-scale, 2D glass micromodels can be used in conjunction with fluorescence microscopy and micro-particle image velocimetry (micro PIV) to directly observe and measure the pore-scale processes (Jiménez-Martínez et al., 2017; Roman et al., 2019, 2016). Roman et al. (2016) investigated the velocity profiles in two-phase flow through the heterogeneous sandstone-replica micromodel using micro PIV. The results depicted recirculation motion inside the immobile pockets of the wetting phase due to momentum transmitted by the flowing oil. Kazemifar et al. (2016) reported shear-induced circulation in trapped water ganglia during post-front passage displacement of water by supercritical CO_2 in a homogenous micromodel. In concordance with the Kazemifar et al. work, Li et al (2017) observed the shear-induced circulation during post-front passage flow in a heterogeneous micromodel for a supercritical CO_2/water system. They determined CO_2 flow directions with the aim of circulation within the trapped water phase, as it is very difficult to directly measure CO_2 flow. Using micro PIV, Heshmati and Piri (2018) observed the recirculation process in a pore-doublet model in the viscous dominant regime. They reported that the shear stress applied to the trapped non-wetting phase was intensified as the viscous

forces increased. The effect of increasing injection velocity on the velocity of the non-wetting phase was less noticeable, indicating the presence of a slip boundary between the fluids. Zarikos et al. (2018) analyzed the interaction of capillarity and momentum transfer between the two immiscible phases for different non-wetting trapped globules with various sizes. In contrast with stagnant areas where the viscous drag applied on the fluid-fluid interface is negligible, in nonzero velocity areas the momentum transfers cause circulations within the trapped phase. The circulation velocity is maximum near the fluid-fluid interface and an increase in capillary number of invading phase increases the circulation velocity as well as the shift in circulation centroid toward high-velocity region. Similar to the circulation phenomenon process for trapped phases in porous media, there are other two-phase systems in which this process is noticeable (Bhaga and Weber, 1981; Maxworthy et al., 1996). The effect of capillary numbers, slug size, and viscosity ratios on internal recirculation within two phases in capillary channels have been investigated in several experimental (Kashid et al., 2007; Liu et al., 2017; Ma et al., 2014) and numerical studies (Kashid et al., 2005; Sarrazin et al., 2006).

Contrary to the recent studies where the velocity fields were observed in only one phase (usually the water phase), two-phase flow can be explored using an appropriate two-phase flow simulator. Pore-network modeling as a low-cost computational tool has advanced during recent years in both quasi-static and dynamic modes (Blunt, 2001; Oren et al., 1998). Direct numerical simulation methods including smoothed particle hydrodynamic (SPH) as a meshless method (Hirschler et al., 2016), the lattice Boltzmann method (LBM) (Kang et al., 2002), and computational fluid dynamic methods (CFD) (Raeini et al., 2012) can perform simulation at high resolution of the real structure of pore spaces. Fakhari et al. (2018) using the lattice Boltzmann model for the simulation of multiphase flows of water/CO_2 systems in a micromodel, observed the recirculating flows in the still-flowing CO_2 phase as the impacts of inertial forces. Direct numerical simulation of pore-scale processes by CFD methods have

gained great prominence due to their ability to simulate fluid flow for wide density and viscosity ratio ranges (Meakin and Tartakovsky, 2009). In a recent study, using direct numerical simulation, the results of drainage processes in a 2D cavity showed better mixing processes and larger interfacial mass transfer in the presence of recirculation inside the cavity (Maes and Soulaine, 2018). Shams et al. (2018) analyzed the viscous coupling effects as a function of the viscosity ratio, wettability, and varying fluid configurations in circular capillary tubes. Raeini et al. (2014) studied the snap-off and layer flow to analyze the impact of geometry and flow rate on the hydraulic conductivity of disconnected ganglia using volume-of-fluid (VOF) based finite-volume method. To consider interfacial tension, various approaches can be applied to VOF; the continuous surface stress (CSS) method (Gueyffier et al., 1999), the continuous surface force (CSF) method (Brackbill et al., 1992), and the sharp surface force (SSF) (Francois et al., 2006; Raeini et al., 2012). In these approaches, it is very difficult to predict flow at low capillary numbers where the capillary forces are dominant, which can result in non-physical velocity currents around the interface (Raeini et al., 2014). To eliminate the non-physical behavior from the numerical solution for the cases of capillary forces dominancy, the filtered surface force (FSF) is introduced (Raeini et al., 2012). Specifically, the capillary pressure, dynamic pressure gradients, and viscous and inertial forces are separately calculated to prevent introducing instabilities in the numerical equations. It is shown that the spurious current is minimum around the interface when the FSF is used (Pavuluri et al., 2018).

The concept and application of the recirculation phenomenon are of great importance especially for processes contending with mass transport (Kazemifar et al., 2016; Li et al., 2017; Maes and Soulaine, 2018). Recently some research has been carried out to investigate this phenomenon in both experimental (Roman et al., 2016; Zarikos et al., 2018) and numerical approaches (Fakhari et al., 2018; Maes and Soulaine, 2018). However, they have not discussed the role of displacement mechanism and fluid configurations on the recirculation process. Also, in the case

of experimental investigations (Kazemifar et al., 2016; Roman et al., 2019, 2016; Zarikos et al., 2018), the velocity profile is only presented inside the trapped phase. Maes et al. (2018) investigated the role of recirculation phenomena on the mass transfer process for various viscosity ratios; however, they did not consider the effects of injection velocity and surface tension as other dynamic parameters involved in the capillary number. Zarikos et al. (2018) investigated how the center of circulation and average velocity of the trapped phase moved for various capillary numbers, but they did not discuss the behavior of capillary number for various viscosity ratios. This work sheds light on the recirculation process for both imbibition and drainage mechanisms for various fluid configurations at low capillary number. Also, using drag force analysis on fluid-fluid and fluid-solid interfaces, we comprehensively discuss the behavior of recirculation phenomena. In addition, we discuss the analysis of dynamic parameters including injection velocity, viscosity ratio, and surface tension individually on the behavior of recirculation.

We used the FSF formulation of the VOF method implemented in poreFoam (separately available solver for OpenFOAM) to simulate two-phase flow inside a 2D pore-doublet model at low capillary number. In this study, we addressed the question of how recirculation behavior changes under various dynamic and static conditions. As the multiphase-flow simulation is carried out in the real structure of pore spaces, this study is new to those that use simplified models such as pore network modeling. Also, using the FSF formulation of the VOF method minimizes the spurious currents introduced in numerical equations. On the other hand, the simulation run time is relatively long due to small time steps that should be used, especially at low capillary numbers. The main limitation is that even with this advanced method, the simulation of fluid flow for the invading phase capillary numbers lower than 10^{-7} cannot be performed. Also, because of high computational cost, investigation of more complex porous

media was not feasible. The increase in mesh size and shortness of time steps might have led to a long simulation time.

The results of this work can be applied for cases where recirculation plays a pivotal role along with mass transfer, such as CO_2 storage. Analyzing drag force on the fluid-fluid interface is also important in processes where the balance of forces on the interface determines the mobilization or trapping of the droplet during enhanced oil recovery methods (Dejam and Hassanzadeh, 2018; Olayiwola and Dejam, 2019; Yang et al., 2020, 2019). Figure 1 is a schematic of the problem statement. This paper is organized as follows: Section 2 presents the numerical method, Section 3 gives the model validation and verification, Section 4 discusses the results, and finally, Section 5 summarizes the conclusions.

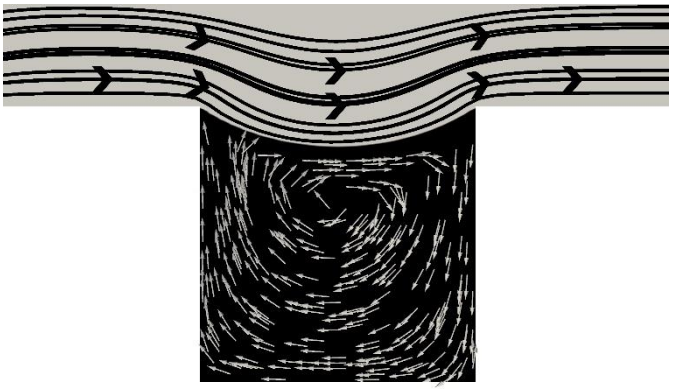

Tool

Volume of Fluid (VOF)

Problem Statement

What is the role of fluids configuration?

How the solid-liquid interface affect the process?

How drag force distribution explains this phenomenon?

How is the velocity distributed through the trapped phase?

Is there a unique effect of capillary number on the recirculation behavior?

Validation

- Phase distributions
- Centroid location
- Velocity distributions on two sides of interface

Figure 1- General Sketch of the problem

2. Numerical Method

2.1. Mathematical Formulation

This section described the mathematical model we used to solve two-phase flow. The Navier-Stokes equation describes the dynamics of two immiscible incompressible flow. Since part of the solutions are interface dynamics, a moving boundary problem is required (Batchelor and Batchelor, 2000). For an isothermal condition, the momentum-balance equation in terms of the viscous, inertial, capillary, and gravity forces is written as (Raeini et al., 2012):

$$\frac{D}{Dt}(\rho \boldsymbol{U}) - \boldsymbol{\nabla}.T = -\boldsymbol{\nabla}P_d + \rho \boldsymbol{g} + \boldsymbol{f}_c - \boldsymbol{\nabla}P_c \quad (1)$$

where **U** denotes the velocity field, ρ the density, t the time, and **g** is gravity vector. $\frac{D}{Dt}(\rho \boldsymbol{U})$ is attributed to the inertial force, which is responsible for the acceleration of fluid and momentum transfer caused by advection. $\boldsymbol{\nabla}.T = \boldsymbol{\nabla}.(\mu \boldsymbol{\nabla U}) + \boldsymbol{\nabla U}.\boldsymbol{\nabla}\mu$ is the viscous force, $\rho \boldsymbol{g}$ is gravity force and $\boldsymbol{f}_c$ is the capillary force. P_d is dynamic pressure and defined as: $P_d = P - P_c$, where the P_c is capillary pressure term. Dynamic pressure is acquired from the mass balance equation in combination with the momentum balance equation, considering incompressible flow:

$$\boldsymbol{\nabla}.\boldsymbol{U} = 0 \quad (2)$$

The capillary pressure term is calculated using the equation:

$$\boldsymbol{\nabla}.\boldsymbol{\nabla}P_c = \boldsymbol{\nabla}.\boldsymbol{f_c} \quad (3)$$

With the boundary condition:

$$\frac{\partial P_c}{\partial n_b} = 0 \quad (4)$$

where n_b is the axis normal to the boundary. Equations (3) and (4) introduce a Neumann problem for capillary pressure term which has a unique solution. Including the effect of the capillary force in Navier-Stokes equations provides an opportunity to filter the instabilities introduced into the numerical equations where the capillary forces are high (Raeini et al., 2012).

At the fluid-fluid interface, the α value is between zero and one. It is evolved with the advection equation of the form:

$$\frac{\partial \alpha}{\partial t} + \boldsymbol{\nabla}.(\alpha \boldsymbol{U}) = 0 \quad (5)$$

By solving Equation 5, the indicator function is obtained then the capillary force f_c can be calculated as a body force (Brackbill et al., 1992):

$$\boldsymbol{f}_c = \sigma k \boldsymbol{n_I} \delta_s \quad (6)$$

where σ is surface tension, $\mathbf{n}_I$ is the unit interface normal vector, δ is the delta function active along the interface and $k = \boldsymbol{\nabla}.(\boldsymbol{n}_I)$ is the interface curvature and is normal to the interface.

$$\boldsymbol{n}_I = \frac{\boldsymbol{\nabla}\alpha}{|\boldsymbol{\nabla}\alpha|} \quad (7)$$

Detailed forced filtered formulation of the volume of fluid method is discussed in appendix A.

2.2. Computational Domain

Two-phase flow simulations were performed in designed 2D pore-doublets, inspired by the Heshmati and Piri (2018) study on velocity fields and shear stress at fluid-fluid interfaces in a controlled environment. Figure 2 shows the 2D geometrical model used in this study. The width of the inlet and outlet of the pore assembly was 120 µm and the model was 410 µm long. This specific model enabled us to examine recirculation inside the trapped phases in various geometrical structures where dead-ends and cavities were designed to resemble the likeliest zones in porous media for the trapping process. The left and right sides of pore-doublet models are cavities perpendicular to the main flow, while in the left side a circular solid provides an opportunity to analyze the rotational flow in the vicinity of solid surfaces. The bottom dead-end is behind the main flow direction, allowing investigation of the recirculation in a zone where the invading phase velocities are relatively low.

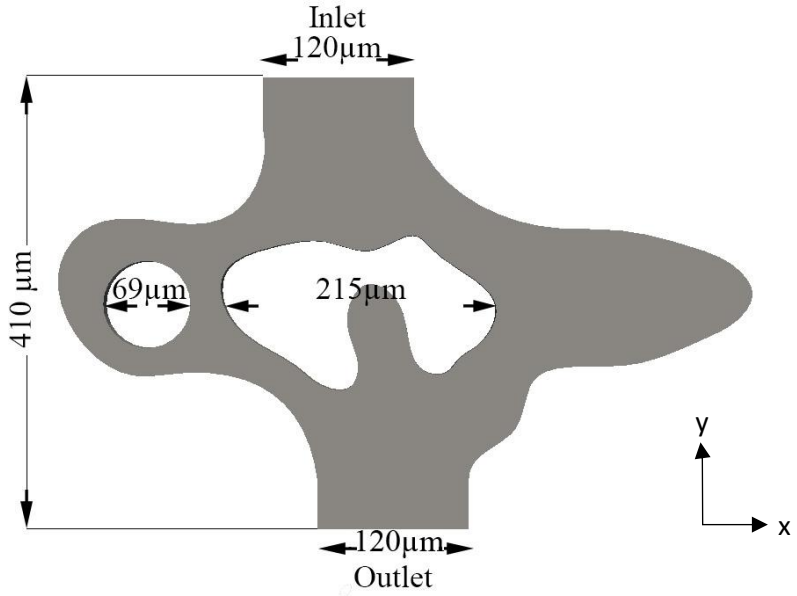

Figure 2 Schematic of the pore-doublet model inspired from Heshmati and Piri (2018)

By subdividing the primary domain into non-overlapping subdomains as smaller discrete cells, flow equations 1-7 and A1-A11 are solved. The domain was meshed using OpenFOAM meshing tools snappyHexMesh (Weller et al., 1998). To visualize the processes, we used Paraview.

2.3. Fluid Properties

To analyze the role of displacement mechanisms on recirculation processes in various fluid configurations inside the pore assembly, we considered a set of fluid properties (Listed in Table 1). The properties were designed to ensure that enough shear stress was transmitted to the trapped phase in both drainage and imbibition mechanisms. To examine the effects of dynamic parameters involving capillary number including surface tension, velocity, and viscosity ratio, different ranges were considered (and explained in that section). As the Bond number ($Bo = \Delta\rho g L/\sigma$, where L is the characteristic length) is equal to zero due to the presence of fluids with the same densities, the effect of gravitational forces is not a focus in this study.

Table 1 Fluid properties

Fluid type	Viscosity (Pa.s)	Density (kg/m^3)	Surface tension (N/m)
Invading phase	0.01	1000	0.03
Trapped phase	0.001	1000	

2.4. Boundary and Initial Condition

One of the essential physical parameters, which should be defined in the numerical solver, is suitable boundary conditions. Zero longitudinal velocity magnitude (U_x) is considered while the imposition of uniform velocity profile equal to 1.0×10^{-4} m/s supplies the latitudinal velocity (U_y) at the inlet. For outlet boundary zero-gauge global pressure, we considered a resemblance with atmospheric pressure. Inlet gradient pressure values and the velocity gradient at the outlet were fixed at zero during all simulations. The grain surfaces predetermined wetting properties depending on the displacement mechanism i.e. fully-wet to the invading phase in the case of imbibition and fully non-wet to the invading phase in the case of drainage. The normal velocity component at a fluid-solid interface was set at zero (no-slip conditions). To analyze the recirculation behavior inside the trapped phases in similar conditions, the model was initially set to be filled with invading fluid then the trapped phase was locally patched at three individual locations on the right and left sides of the pore assembly and around the bottom dead-end. Then the invading fluid with a certain contact angle depending on the displacement mechanism (i.e. zero for imbibition and 180º for drainage) was injected at the inlet.

2.5. Solution Methodology

For a time-dependent approach for 2D simulations, an open-source finite volume CFD package was used. The FSF formulation of the VOF method (Raeini et al., 2012) with pressure implicit-

split operator (PISO) algorithms (Issa, 1986) was a segregated procedure used to solve the pressure, velocity and volume fraction coupling equations. We used a semi-implicit formulation of capillary forces to confirm the accuracy and stability of the numerical method. Adjustable time-steps with a maximum courant number of 1.0×10^{-5} (Ferziger and Perić, 2002) were used. The time steps were designed in a way to satisfy the constraints below (Raeini et al., 2012):

$$\delta t < C_{\delta t}\frac{\mu \delta x}{\sigma} \qquad 8$$

where δt is time-step size, δx is mesh resolution, and C_{st} is a constant varying depending on the formulation of capillary forces (explicit or semi-implicit) (Raeini et al., 2012). The simulations in this work were performed on Intel Core i9, 5 GHz, 16 MB cache with 16 processors and 16 GB RAM.

3. Validation and Verification

3.1. Mesh Independency

The mesh density of the network is governed in a way that no dependency between the discretization and variable can be observed. The OpenFOAM snappyHexMesh utility was used for domain meshing. This tool allows good refinement of grids in the various parts of a pore assembly. The mesh quality was confirmed by analysis of grid refinement, where numbers of mesh elements were increased gradually from 8800 to 79,000, corresponding to the number of cells in the narrowest throat from 9 to 11, 13, and up to 23. The residuals, average velocity, and velocity distributions inside the sub-domains were calculated in each simulation to confirm the grid-size convergence. The results showed that the simulation with 19 cells in the narrowest throat equivalent to a mesh size of 55,635 cells led to minimum error while the finer mesh did not decrease the error. Figure 3 illustrates the mesh inside the pore assembly.

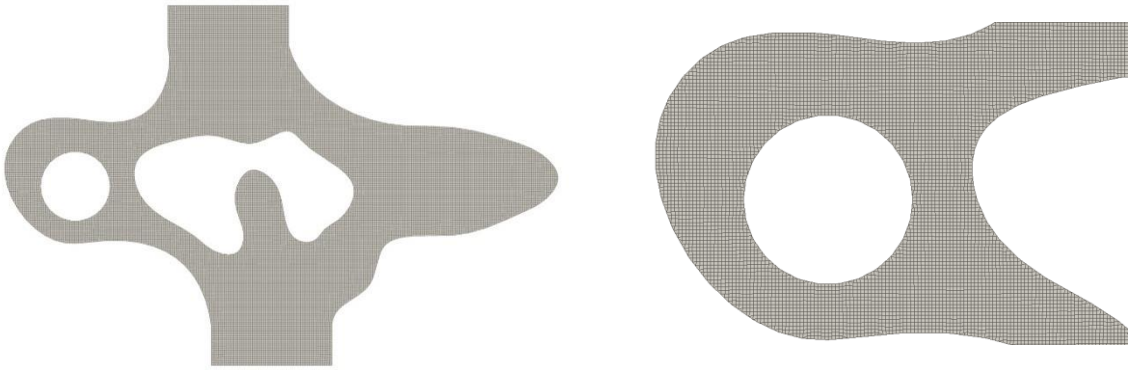

(a) (b)

Figure 3 Demonstration of mesh inside (a) the pore assembly, and (b) the left-hand cavity

4. Results

This section considers the simulation results of two individual displacement mechanisms i.e. imbibition and drainage through the pore-doublet model. In both cases three patches of defending phase were trapped in the right and left sides of the pore-doublet model as well as the bottom dead-end. This fluid configuration within the pore assembly not only facilitated the analysis of recirculation behavior in various arrangements to the flow direction but also provided the same conditions for both displacement mechanisms. Prior to any displacement simulation, the trapped patches were relaxed for 0.03 s to remove the capillary oscillation effects from the numerical calculations. During this process, no inflow or outflow of the fluids across the boundaries was considered, to make the interface reaching equilibrium configuration depending on the contact angle. Then the displacement process was simulated to reach the steady-state condition, depending on the displacement mechanism.

4.1. Model Validation

To ensure the accuracy of the numerical model, the simulation results were validated with available experimental data mentioned in the study of Heshmati and Piri (2018) (Heshmati and Piri, 2018). They analyzed the recirculation process inside one side of a pore-doublet model (originally inspired by Chatzis and Dullien (1983)) for immiscible displacement. Table 2 shows

the values for velocities at 10 μm intervals to the liquid-liquid interface inside invading and trapped phases. Our simulation results show that in a similar boundary and initial conditions to their experimental study, a recirculation zone was created inside the non-wetting trapped phase at the right side of pore assembly. Analysis of velocity distribution at both sides of liquid-liquid interface shows that the velocities are in good agreement with the experiment. Due to the low quality of images in Heshmati and Piri, (2018), we validated this process using other experimental data. We used the experimental data related to a drainage process inside dead-end pore micromodels (i.e. eddy pockets) (Roman et al., 2019). To simulate the drainage mechanism eddy pockets including three connected cavities were considered (Figure 4 (a)), then with the same boundary and initial conditions to their experimental study the non-wetting phase was injected through the micromodel. To avoid the borders effect, the central cavity results were selected to be compared with the experimental results. A mesh sensitivity was performed and mesh size equal to 93,600 cells (equivalent to cell size of 1.6 micron) was selected as the optimum density. As Figure 4 (b) shows, good agreement can be seen between the numerical simulation and experimental results, especially in phase distributions and the velocity profile inside the cavity. To better understand the velocity distribution inside the trapped phase, the values of Ux and Uy along the vertical axis to the centroid (dashed white line in Figure 4 (b,c)) for the simulation process are compared with the experimental result. The values of Uy are near zero for both experimental and simulation approaches. As can be seen in Figure 5 for Ux values, although the trends of experimental and simulation results are in concordance. There is only a minor change in the locations of the centroid (Ux=0) that can be attributed to the effect of differences in the degree of the sharpness of the corners in experimental and simulation analysis.

Table 2 Comparison of velocities near the interface inside the invading and trapped phases in experimental and modelling approaches

Approach	Velocity inside wetting invading phase (10 µm far from the interface) (m/s)	Velocity inside non-wetting trapped phase (10 µm far from the interface) (m/s)	Velocity ratio (invading to trapped)
Experimental results (Heshmati and Piri, 2018)	110 (µm/s)	21 (µm/s)	5.2
Modelling results (this study)	99 (µm/s)	23 (µm/s)	4.3

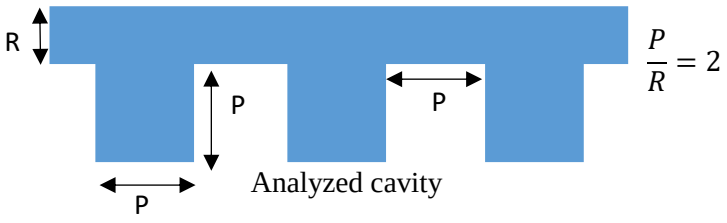

(a)

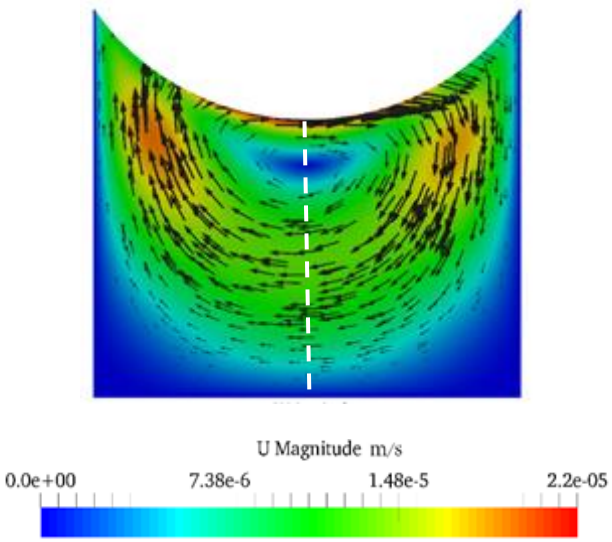

(b)

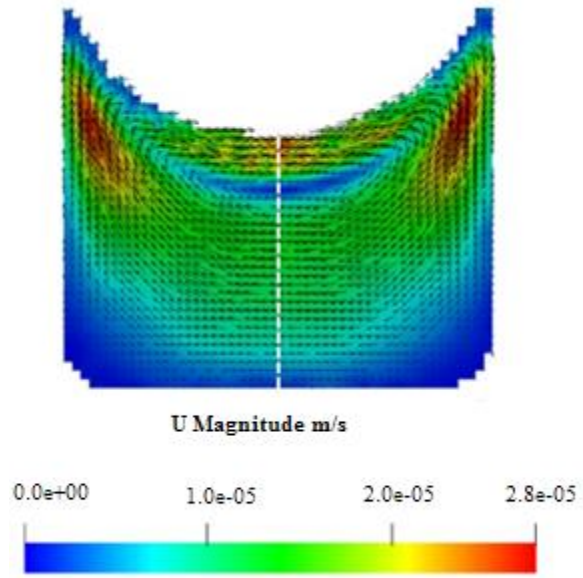

(c)

Figure 4 Comparison of phase distribution and velocity profile for a trapped phase inside the cavity during the drainage process: (a) Schematic of location of analyzed cavity inside the eddy pockets (Roman et al., 2019), (b) Simulation results, and (c) Experimental results from (Roman et al., 2019)

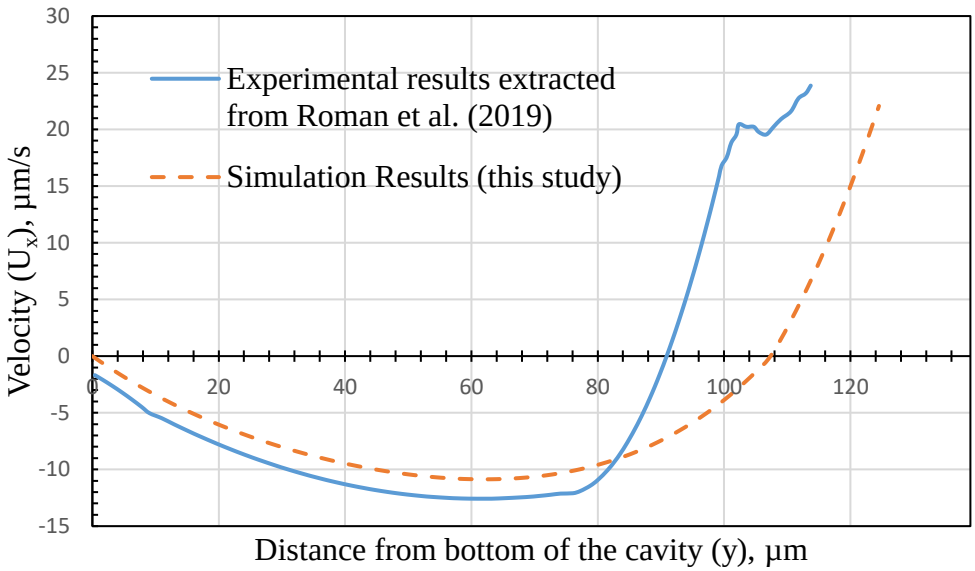

Figure 5 Velocity profile along the vertical axis (dashed white line in Figure 4) to the centroid of recirculation from the bottom of the cavity to the fluid-fluid interface

4.2. Displacement Mechanisms and Fluid Configurations

Displacement mechanisms can play a pivotal role in the forces acting on the phase interface leading to change in interface shape. To assess recirculation behavior in various displacement mechanisms, imbibition, and drainage mechanisms within pore-doublet models were simulated at the same injection velocity, 100 µm/s. Figure 6 shows the fluid configuration and velocity field through the pore-doublet model for both cases. The blue phase is wetting and the orange is non-wetting; the tubes show the velocity intensity through the invading phase and arrows depict the direction of flow through the trapped phase. Depending on the configuration of the fluids to the flow direction, the counter clockwise or clockwise recirculation inside the trapped phase is formed (Zarikos et al., 2018). This rotational flow is attributed to the shear stress transmitted at the interface of the fluids. In contrast to the imbibition case, the trapped phase has a concavity shape in the drainage mechanism where two tails of the wetting phase are

elongated along the solid wall. Some research has been conducted to observe the characteristics of rotational flow during this mechanism in complex 2D porous media (Fakhari et al., 2018; Kazemifar et al., 2016; Li et al., 2017). Here the focus was on the various pore structures combined in a pore assembly to assess the recirculation process at low velocity. Using Equation 9, the capillary number of invading phase was calculated, where U_i is invading phase velocity, μ_i is invading phase viscosity, and σ is surface tension. The calculated Ca_i was around 3.3×10^{-5} and M, viscosity ratio, was 10.

$$Ca_i = \frac{U_i \mu_i}{\sigma} \qquad 9$$

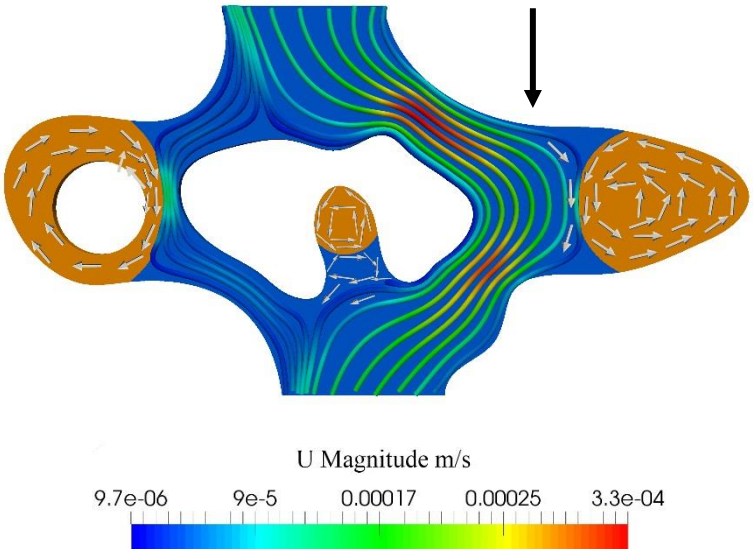

(a)

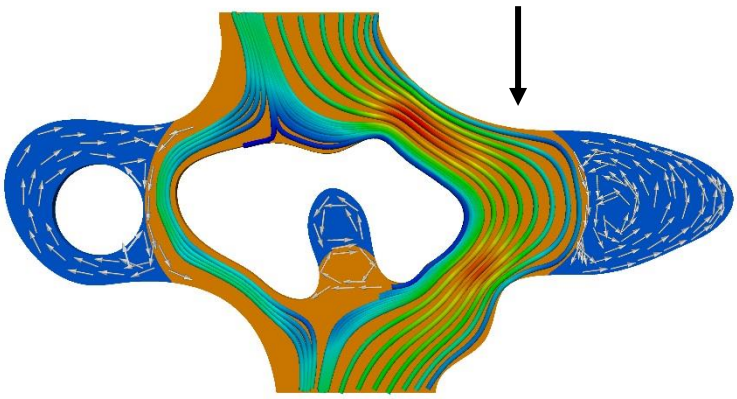

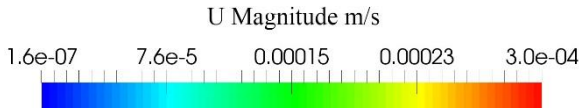

(b)

Figure 6 Velocity profiles and fluid distributions through the pore-doublet model during, Ca≈3.3×10 $^{-5}$, M=10: (a) Imbibition mechanism, and (b) Drainage mechanism (The blue and orange colors represent the wetting and non-wetting phases respectively, the black arrows show the direction of main flow and color tubes show velocity magnitude.)

4.2.1. Right-hand Cavity (Perpendicular to the Mean Flow Direction)

The cavity located on the right side of the pore-doublet model resembles a T-junction geometry to the mean flow direction. Figure 7 depicts the fluid distribution and velocity vectors on the right side of the pore assembly for both imbibition and drainage mechanisms. While the arrows show a counter-clockwise flow direction through the trapped phase, the color tube illustrates the velocity inside the trapped phase where a zero velocity zone was formed at the centroid of the recirculation region. In the case of the imbibition mechanism, because the non-wetting phase was trapped at the end of the right side, a convex meniscus was formed at the fluid interface. At the upper and lower sides of the interface inside the invading phase in the right side of pore assembly there were two zero velocity zones proving the presence of two stagnant regions, which are shown by red circles in Figure 7 (a). In the case of the drainage mechanism, we observed no stagnant zones inside the invading fluid near the fluid-fluid interface, which is attributed to the recirculation inside the wetting phase even at two tails elongated at solid walls.

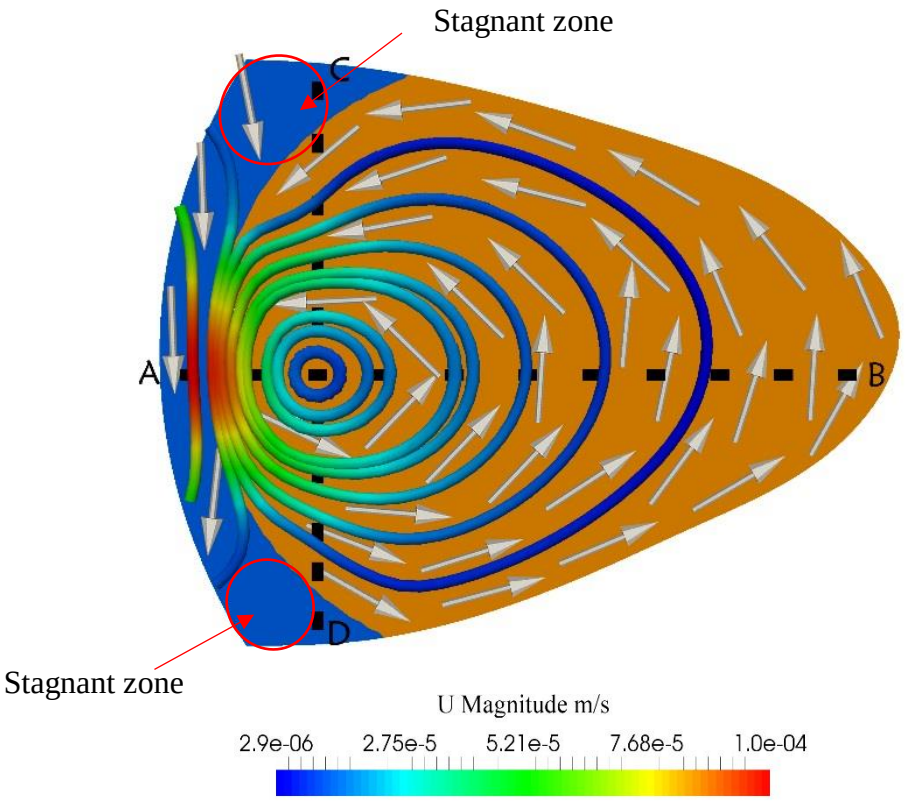

(a)

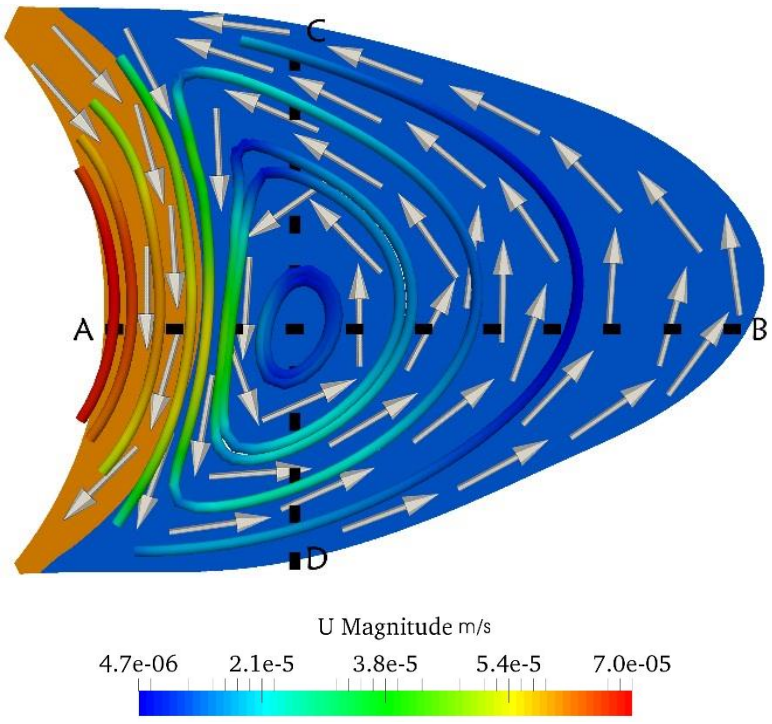

(b)

Figure 7 Velocity field through the recirculation zone inside the trapped phase at the right side of the pore assembly: (a) Imbibition mechanism, and (b) Drainage mechanism (The blue and

orange colors represent the wetting and non-wetting phases respectively, the red circles are the stagnate zones, and the white arrows show direction flow inside the trapped and flowing phases.)

To analyze the velocity distribution inside the trapped phase, the fluid velocity curves along the vertical and horizontal axis to the centroid of the trapped phase are shown in Figures 8 and 9, marked by black dashed lines in Figure 7. Figure 8 demonstrates the fluid velocity curves; U_x, $U_{y,}$ and velocity magnitude (U_{mag}), along the horizontal axis to the centroid of the trapped phase for both imbibition and drainage mechanisms shown by horizontal black-dashed lines from point A to B in Figure 7. Similar velocity field behavior was observed in both cases, while changes in velocity magnitude trends at the fluid-fluid interface were more noticeable in drainage displacement. U_y is significantly higher than U_x, so U_{mag} is mostly affected by the U_y value. Whereas the changes in U_y values show a change in flow direction within the trapped phase, showing the location of the centroid in the trapped phase. The presence of interface changes in the slope of the profile velocity (Heshmati and Piri, 2018). The zero velocity zone is detected at the recirculation centroid inside the trapped phase and moved toward the wall for the drainage case. No symmetry in the velocity field around the centroid can be seen, since the phase distribution is not the same on the right and left sides of the centroid.

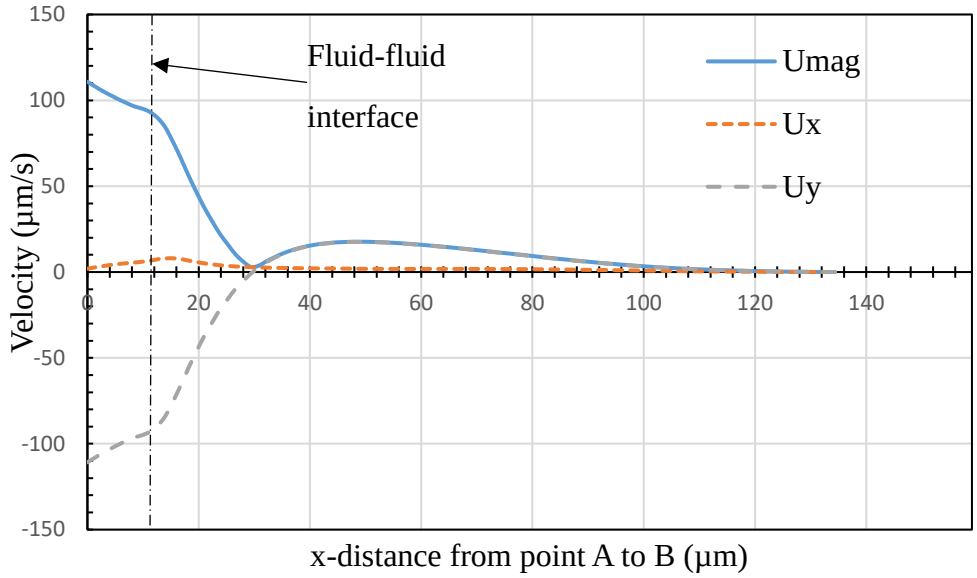

(a)

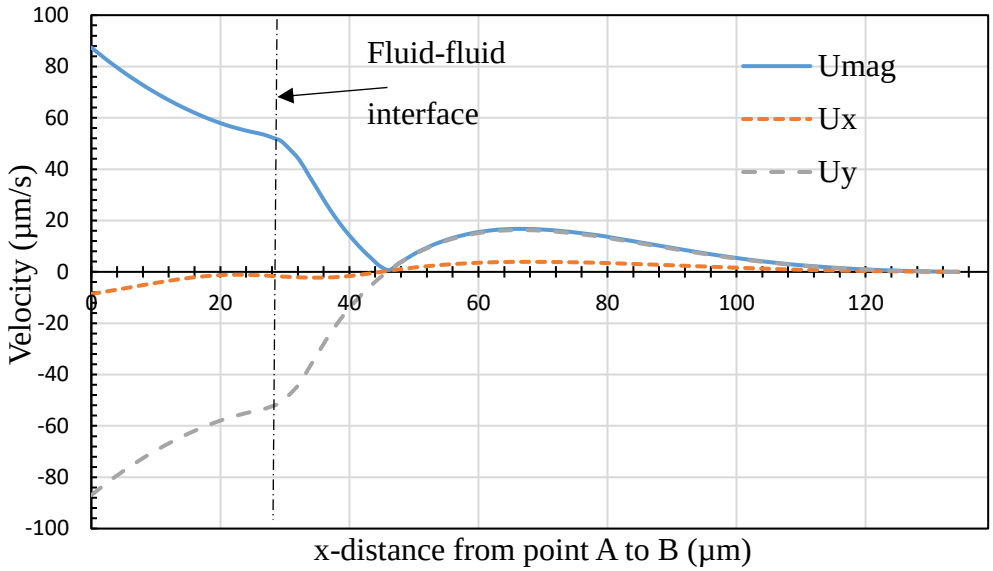

(b)

Figure 8 Velocity profiles along the horizontal axis at the right side of the pore assembly: (a) Imbibition mechanism, and (b) Drainage mechanism (Dotted vertical lines demonstrate fluid-fluid interface)

Figure 9 demonstrates the fluid velocity curves along the vertical axis relative to the trapped phase centroid shown by vertical black-dashed lines in Figure 7. The trend of the U_{mag} curve along the vertical axis has an M shape, an increase immediately after the upper interface, a decrease close to the centroid, an increase as it moves away from the centroid, and finally a

decrease toward the solid wall. In the case of imbibition mechanism, the sharp change in the U_{mag} curve at early microns expresses how interface occurs, in such a way that the velocity value inside the recirculating trapped phase is one order of magnitude higher than those in stagnant zones inside the invading phase. As the viscosity of the trapped phase is noticeably lower than the invading phase, the momentum transfer cannot cause a vortex inside the stagnant zones. The U_y values are fully negative along the vertical axis as the flow is downward along the vertical axis. On the contrary, during drainage displacements, the main flow of the invading phase collides between the interface as the trapped phase is stretched on the solid surface at both the upper and lower sides of the interface. It led to the formation of a more elongated centroid resulting in positive U_y between the vertical axis. Also, no stagnant regions can be detected as the vertical axis to the centroid fell completely into the trapped phase. Distribution of the velocity inside the trapped and invading phases near the interface can be better understood in the surface velocity plots presented in figures in the appendices.

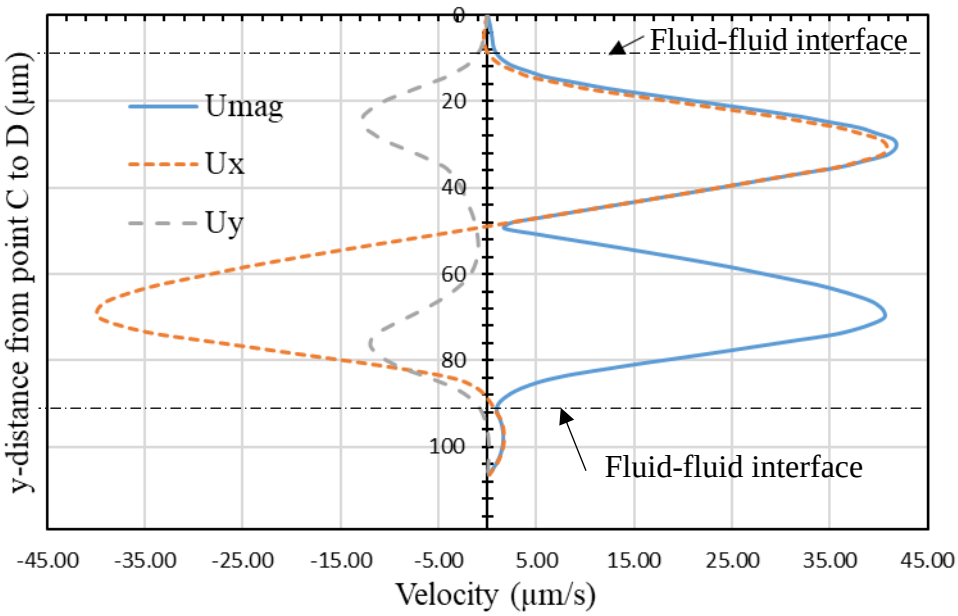

(a)

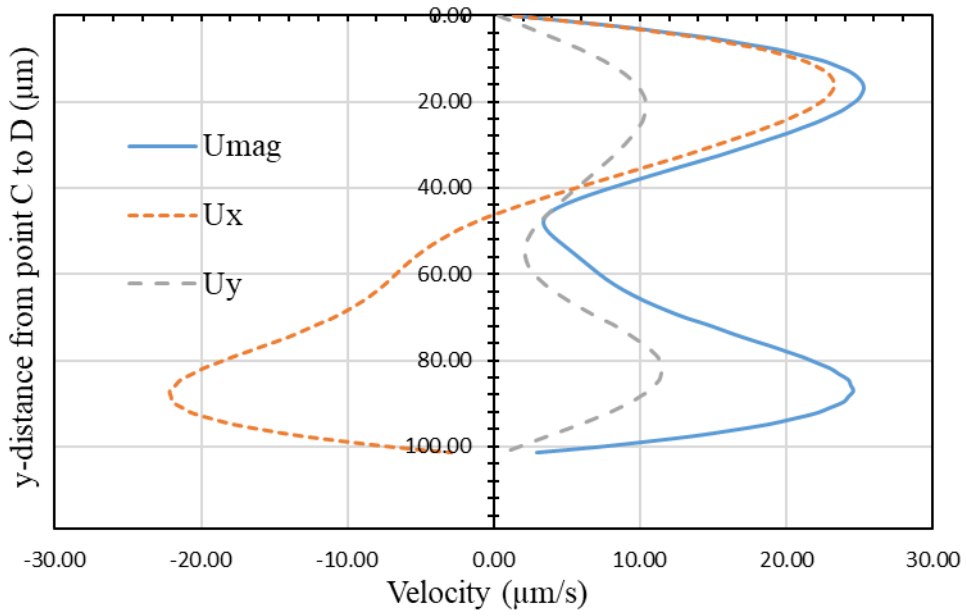

(b)

Figure 9 Velocity profiles along the vertical axis at the right side of pore assembly: (a) Imbibition mechanism, and (b) Drainage mechanism (Dotted horizontal line in part (a) demonstrates fluid-fluid interface)

4.2.2. Left-hand Cavity (vicinity of solid-liquid interface to the liquid-liquid interface)

The cavity on the left side of the pore-doublet model helps us understand recirculation behavior where the solid surface is near the liquid-liquid interface. Figure 12 illustrates the fluids distribution and velocity vectors on the left side of the pore assembly for both displacement mechanisms. In the case of the imbibition mechanism, part of the adjacent throat close to the circular solid surface is filled by the non-wetting trapped phase while the rest is occupied by the flowing wetting phase. The convexity of the trapped phase inside the throat, as well as the circular solid surface close to the interface, caused a small clockwise recirculation through the narrow layer of the non-wetting phase inside the throat. The black arrows show a reverse direction of flow in this zone. This recirculation is followed by a vast circulation inside the cavity and around the circular solid. Similar to the right side of the pore assembly, two stagnant regions in the upper and lower parts of the trapped non-wetting phase are shown by two red

circles in Figure 10(a). On the other hand, during drainage displacement, the layer of the trapped phase inside the throat is rather thin. The low thickness of the trapped phase within the throat, the concavity of the trapped phase, and the existence of a solid surface in the vicinity of fluid-fluid interfaces result in the creation of two individual centroids with clockwise circulation. The reverse direction of flow near the solid surface in these zones is shown by the black direction in Figure 10(b). The wetting layer adhered to the solid surface is so thin inside the throat that a complete circulation around the circular solid surface cannot be seen; consequently, two centroids upper and lower of the thin layer are formed.

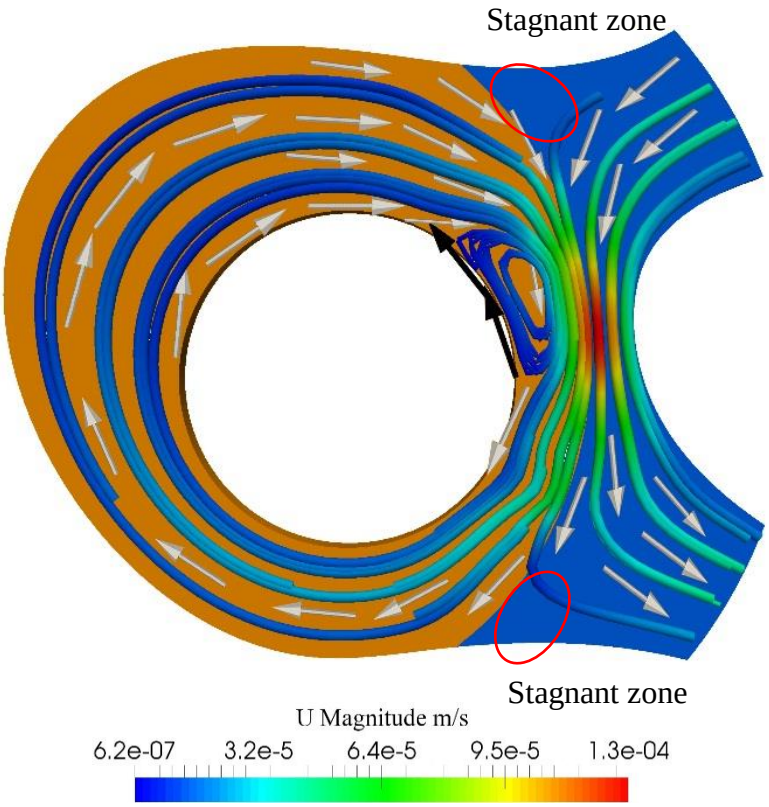

(a)

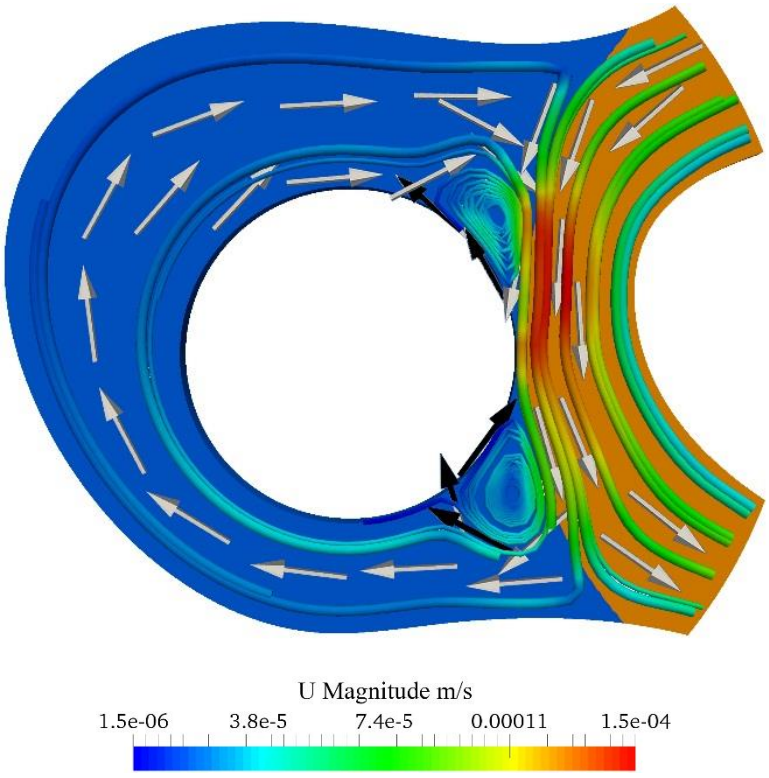

(b)

Figure 10 Velocity field through the recirculation zone inside the trapped phase at the left side of the pore assembly: (a) Imbibition mechanism, and (b) Drainage mechanism (The blue and orange colors represent the wetting and non-wetting phases respectively, the white arrows show direction flow inside the trapped and flowing phases, the red circles are the stagnate zones, and the black arrows show the reverse direction of flow in the vicinity of solid surface and recirculation zone.)

4.2.3. Bottom Dead-End (behind the mean flow direction)

The presence of the bottom dead-end makes it possible to examine recirculation behavior inside a trapped phase in a location behind the mean flow direction. Figure 11 shows the fluid configuration and velocity fields in the bottom dead-end of the pore assembly. In contrast to two other cases, the dead-end is not fully trapped, and around half of it is occupied by the invading phase. This offers a chance to the invading phase to circulate inside the dead-end in both cases. Although in some studies more than one vortex is observed in a trapped phase

(Kashid et al., 2005; Liu et al., 2017; Zarikos et al., 2018), here two adjacent circulations coexist in invading and trapped phases. The circulation of the invading phase transfers enough shear stress to the trapped phase, causing recirculation. The recirculation directions are opposite inside the invading and trapped phases present at the dead-end, clockwise inside invading fluid and counter-clockwise within the trapped phase. Analogous to two other cases, during imbibition mechanism stagnant areas are formed inside the invading wetting phase adjacent to the liquid-liquid and solid-liquid interfaces. Distribution of the velocity inside the trapped phase and invading phase near the interface can be better understood in the surface plots of velocity for various fluid configurations, presented in Figures B1-3 in the appendix.

(a)

(b)

Figure 11 Velocity field through the recirculation zone inside the trapped phase at the bottom dead-end of the pore assembly: (a) Imbibition mechanism, and (b) Drainage mechanism (The blue and orange colors represent the wetting and non-wetting phases respectively and the white arrows show direction flow inside the trapped and flowing phases.)

4.3. Drag-Force Analysis

Our goal is to quantify and analyze the velocity distributions inside the recirculating trapped phase in both imbibition and drainage mechanisms. Detailed velocity fields near the fluid-fluid interface are used for drag-force quantification (Zarikos et al., 2018). The drag-force analysis helps us better understand recirculation behavior for various fluid configurations as well as the displacement mechanism. Viscous drag force per unit of the depth of interface exerted on each part of the interface is calculated as:

$$D = \mathrm{n}.\,\mu_{\mathrm{i}}\left(\frac{\partial \mathbf{u_x}}{\partial \mathrm{y}} + \frac{\partial \mathbf{u_y}}{\partial \mathrm{x}}\right)\mathrm{dl} \qquad 10$$

Where *D* is drag force per unit of the depth of interface, n is the normal vector, μ_i is the viscosity of the invading phase, and l is the interface length. The distribution of drag force per unit of interface depth for the right-side cavity is shown in Figure 12. It clearly shows that in the case of imbibition, the maximum drag force from the invading phase is exerted around the center of the interface, while in two stagnant regions at the upper and lower sides of the interface inside the invading phase, drag force has a reverse direction. It shows that in these areas the force is exerted from the recirculating trapped phase; however, it cannot cause recirculation inside the invading phase as the invading phase viscosity is noticeably high. In contrast, in the case of the drainage mechanism, drag force is at a minimum around the central parts of the interface and an increase can be seen by moving toward the upper and lower sides of the interface. This drag-force distribution along the interface directly affects the centroid shape inside the recirculating trapped phase. The values for the centroid elongation factor, which is defined as the parallel diameter of centroid to the interface divided by the perpendicular one, are 1.11 and 2.76 for imbibition and drainage mechanisms respectively. It proves that the more the drag force is exerted on the upper and lower sides of the interface the more elongation factor of the centroid is obtained.

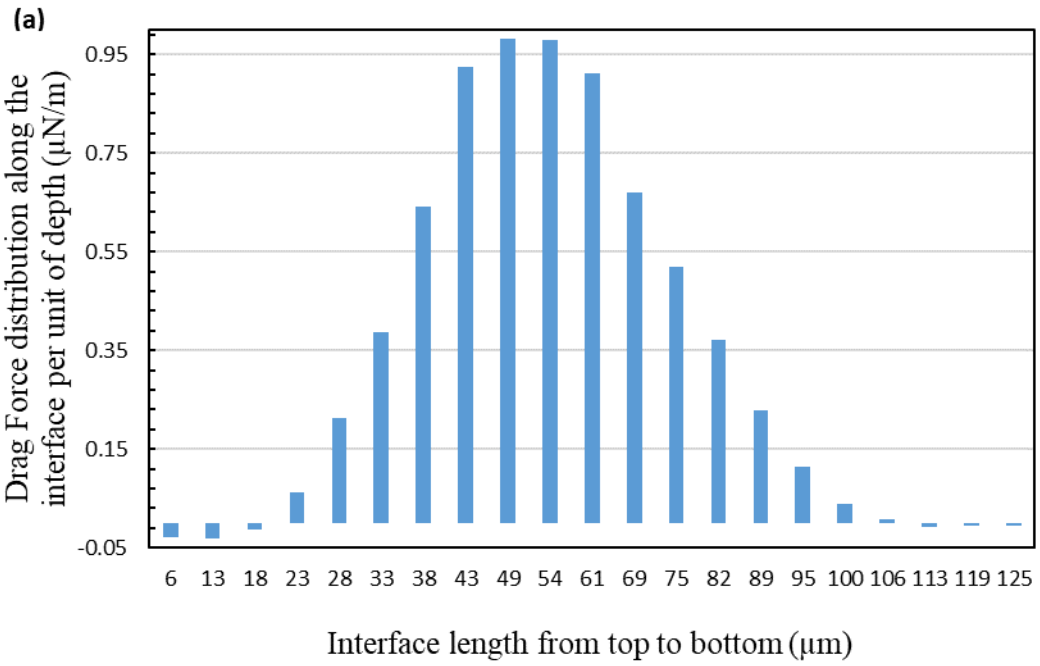

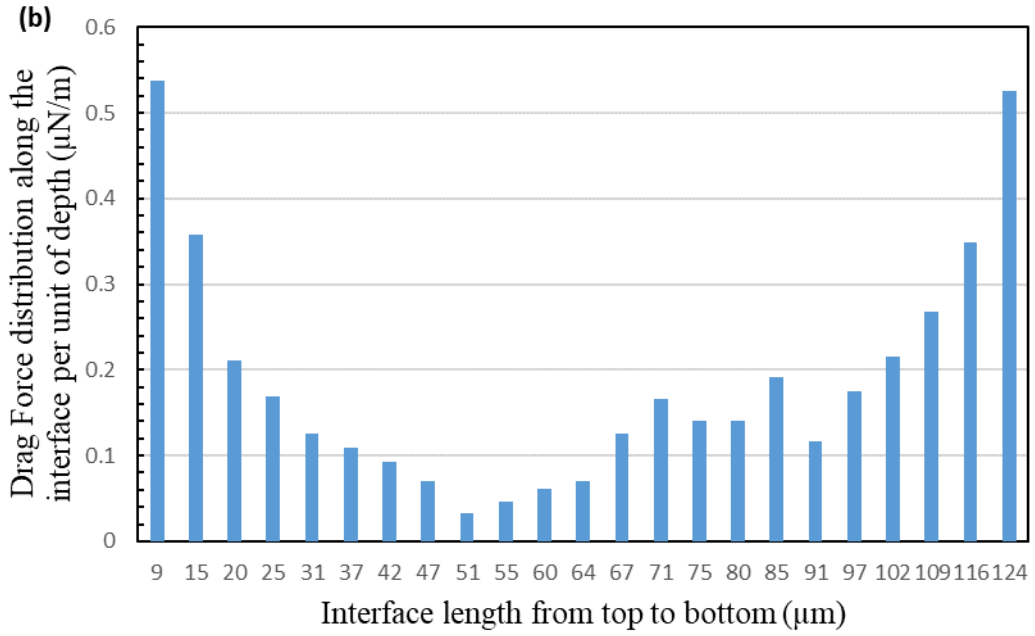

Figure 12 Drag-force distribution along the interface per unit of depth (µN/m) at the right-hand cavity: (a) Imbibition mechanism, and (b) Drainage mechanism

The average velocities inside the recirculation trapped zone for drainage and imbibition mechanisms were 12.36 µm/s and 10 µm/s respectively. This shows that the presence of two stagnant zones during the imbibition mechanism leads to less intensified recirculation. In other

words, less interface is exposed to the high velocity invading phase during imbibition displacement.

For a better understanding of recirculation behavior near the solid surface, drag-force distribution along the right side of the solid circle (close to the interface) inside the left-hand cavity (Figure 10) was analyzed and is shown in Figure 13. The remarkable point is that immediately before and after the center of circulations, two stagnant zones with minimized drag force exerted on the solid circle exist for both imbibition and drainage mechanisms. The drag-force values were higher for the lower part of the semicircle as the radius of the channel around the circle was lower leading to higher velocities. For the drainage mechanism, the drag force suddenly increased at the central part of the semicircle, where the thickness of the trapped layer was significantly decreased. The drag force applied on the semicircle, in the case of the drainage mechanism, was higher as the average velocities inside the trapped zones were 22.46 and 13.55 µm/s, for drainage and imbibition displacements respectively.

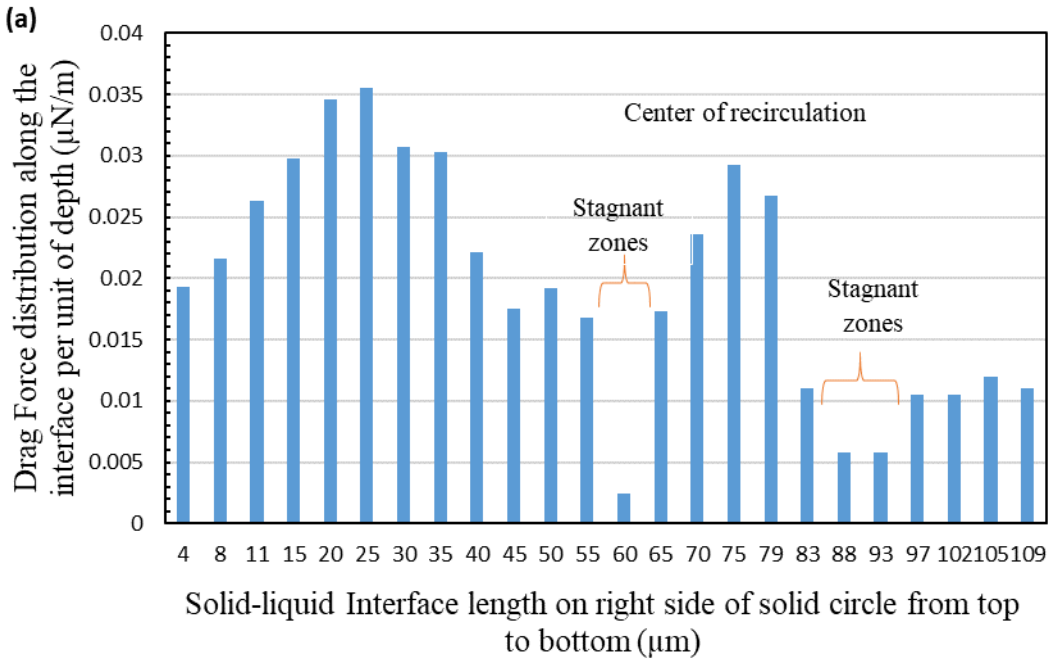

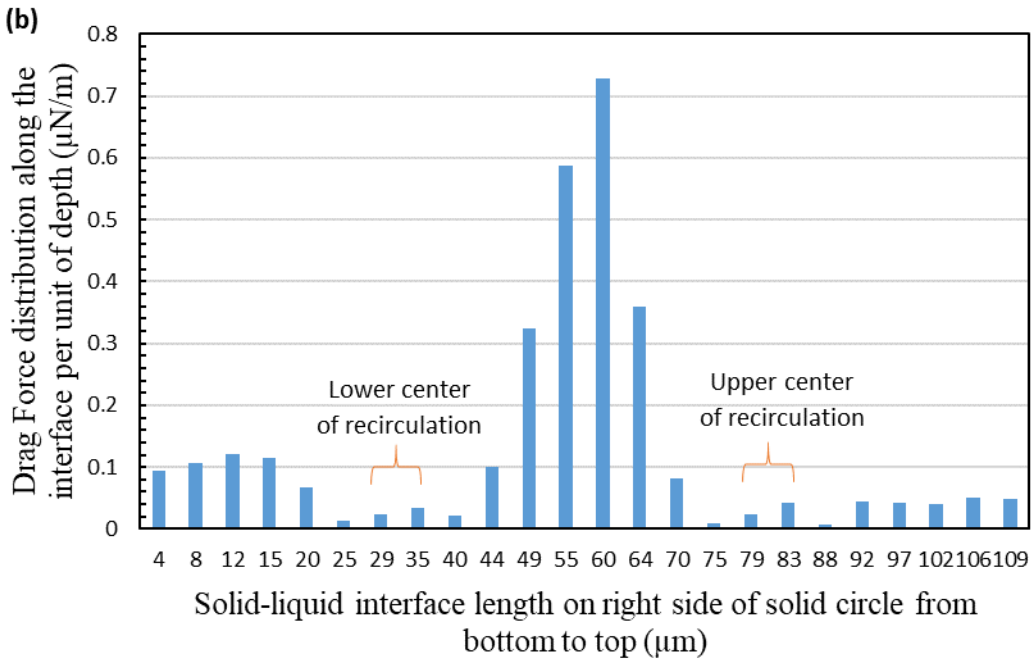

Figure 13 Drag-force distribution along the right side of the solid circle surface per unit of depth (µN/m) at the left-hand cavity: (a) Imbibition mechanism, and (b) Drainage mechanism

Analysis of drag-force distribution along the interface for bottom dead-end depicted in Figure 14 shows similar behavior to the other two cases. Although the recirculation of the invading phase in the vicinity of the trapped phase provides enough shear stress to recirculate the trapped phase, this was not sufficient to cause intensified circulation. Analysis of average velocities inside the trapped phase reveals that the velocities inside the trapped phase at the bottom dead-end were two orders of magnitude less than the cavities. The elongation factors for centroids of rotation were 0.66 and 1.44 for imbibition and drainage respectively. This is consistent with the results for the drainage mechanism in right-hand cavity. The more drag force exerted on two elongated tails of trapped phase on the solid surface (on which the trapped phase is adhered) results in higher elongation factor of the centroid.

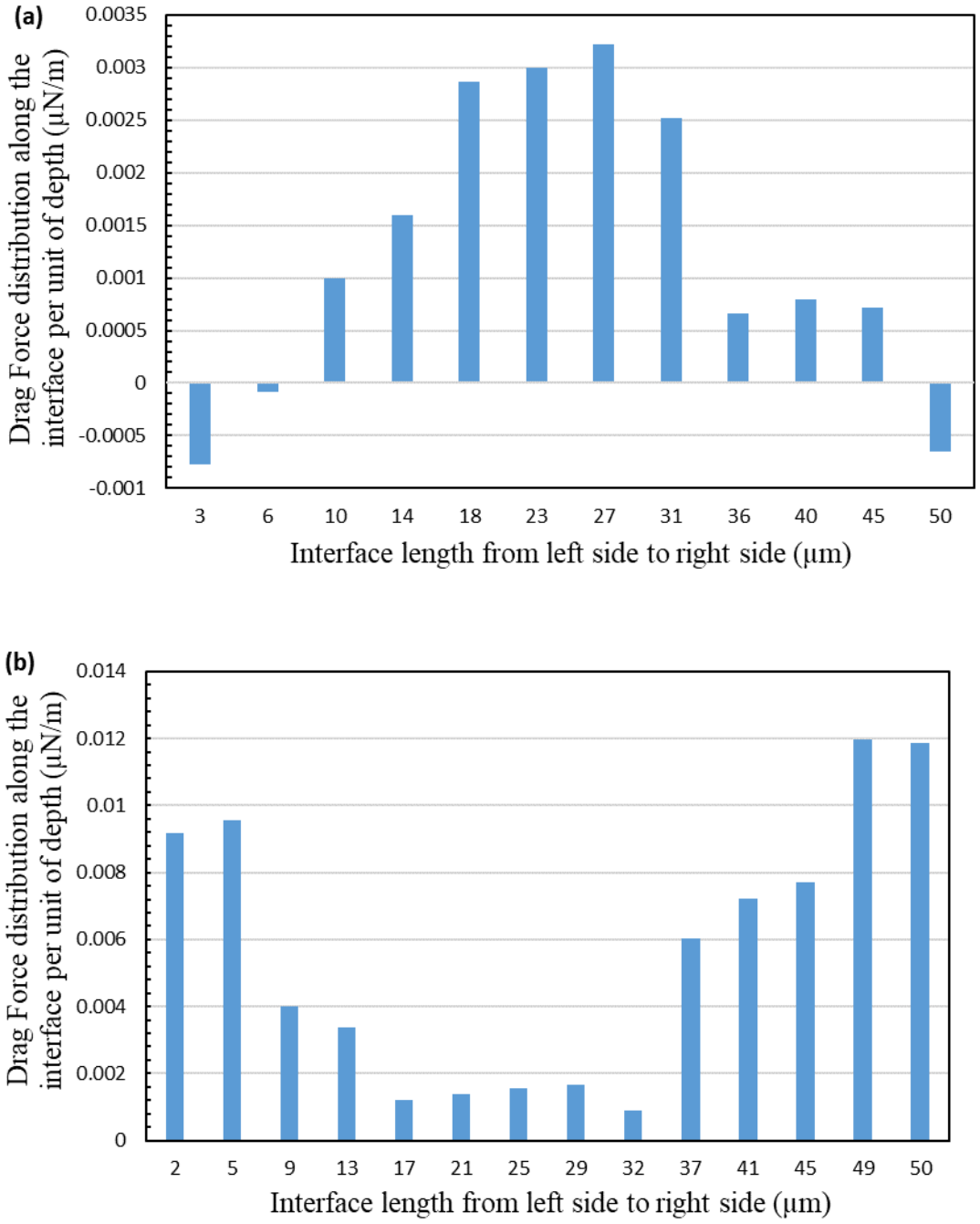

Figure 14 Drag-force distribution along the interface per unit of depth (µN/m) at bottom dead-end: (a) Imbibition mechanism, and (b) Drainage mechanism

The detailed average velocities of trapped phases are shown in Table 3, where the effects of displacement mechanism and fluid configuration on average velocities are obvious. The higher average velocity inside the trapped phase is seen in the case of drainage compared to imbibition. The average velocity was at a maximum for the left-side cavity where the narrowness of the

throat resulted in high momentum transfer from the invading phase to the trapped one. The minimum average velocity inside the trapped phase was at the bottom dead-end, which was behind the mean flow direction. Consequently, the least momentum was transferred to the trapped phase.

Table 3 Average velocity inside the trapped phase for different fluid configurations and various displacement mechanisms

Displacement Mechanism	Average Velocity inside the recirculating trapped zone (μm/s)		
	Right-side Cavity	Left-side Cavity	Bottom dead-end
Drainage	12.4	22.5	0.7
Imbibition	10.0	13.5	0.1

Another factor that is of great importance is the volume of the trapped phase normalized by interfacial area, V_{trap}/A_{int}, listed in Table 4 for various cases. This parameter can give a good sense of the dispersion of the drag force through the trapped phase. Although the values of V_{trap}/A_{int} are slightly higher for the drainage mechanism, the more intensified recirculation can be seen in these cases. This is because of greater accessibility to the interfacial area during drainage as no stagnant zones exist near the interface. The point that draws attention to itself is that the V_{trap}/A_{int} was lowest in the bottom dead-end alongside the minimum average velocity. As the bottom dead-end was behind the mean flow direction, the drag force exerted on the interface was low. This decreased the average velocity inside the trapped phase in bottom dead-end in comparison to two other locations in pore assembly even in the case of low V_{trap}/A_{int}.

Table 4 Volume of the trapped phase normalized by interfacial area for different fluid configurations and various displacement mechanisms

Displacement Mechanism	Volume of the trapped phase normalized by interfacial area (μm)		
	Right-side Cavity	Left-side Cavity	Bottom dead-end
Drainage	72	63	50
Imbibition	70	63	48

4.4. Effect of Fluid Dynamic Properties on Recirculation Behavior

Although experimental and numerical studies have analyzed the role of capillary forces and viscosity ratio on the mobilization of the trapped phase as well as the recirculation intensity inside the trapped ganglia (Kashid et al., 2007, 2005; Liu et al., 2017; Ma et al., 2014). However, the effects of parameters incorporating in capillary number of invading and trapped phases ($Ca_i = \frac{V_i \mu_i}{\sigma}$ & $Ca_t = \frac{U_t \mu_t}{\sigma}$) and the viscosity ratio on the movement of the center of rotation and average velocity of the recirculating trapped zone are not well discussed in the available literature. Here we analyze recirculation behavior under various dynamic conditions.

4.4.1. Viscosity Ratio

Li et al. (2015) investigated the effect of viscosity ratio at a constant Reynolds number on the velocity field inside a spherical droplet exposed to shear flow. They observed that depending on the viscosity ratio a change in location of the source points (centroids of recirculation) can be seen. In this case, we investigated the effect of viscosity ratio on the recirculation performance at a low capillary number. To understand the role of viscosity ratio, diverse viscosity ratio ranges for various cases including water/polymer solution-heavy oil displacement in porous media ($M = \frac{\mu_i}{\mu_t}$) from 1/100 to 100 were considered during an imbibition displacement through the pore-doublet model where a non-wetting phase was patched only on the right-hand cavity. The constant injection velocity was 1×10^{-4} m/s and surface tension of

0.05 N/m. As the vertical movements of centers of rotations for different viscosity ratios are negligible, the changes in the horizontal location of centroids to the basis case (M=1) are shown in Figure 15. By deviating the viscosity ratio from unity to the higher or lower ones, the centroids shift to the right. The more the invading viscosity, the more drag force is exerted on the interface, pushing the interface to the right side. On the other hand, as the viscosity of the trapped phase increases, the more energy is dissipated through the trapped phase (Pilotti et al., 2002). Consequently, although the interface moves to the left (due to the change in drag-force balance) the dissipation results in the movement of centroid to the right. In Figure 16 the change in the average velocity of the trapped phase versus the viscosity ratio is shown. It illustrates that by increasing the viscosity ratio, the average velocity inside the trapping phase logarithmically increases. This logarithmic behavior can be attributed to the coupled effects of changes in transmitted shear stress, dissipation of energy inside the trapped phase and movement of centroid.

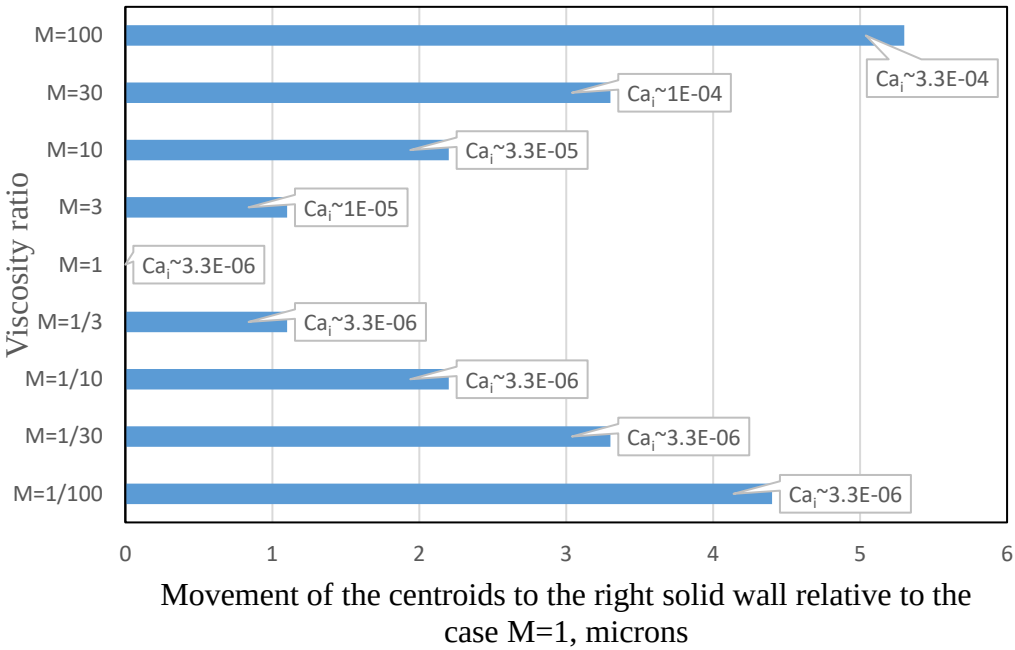

Figure 15 Changes in the location of centroids for different viscosity ratio

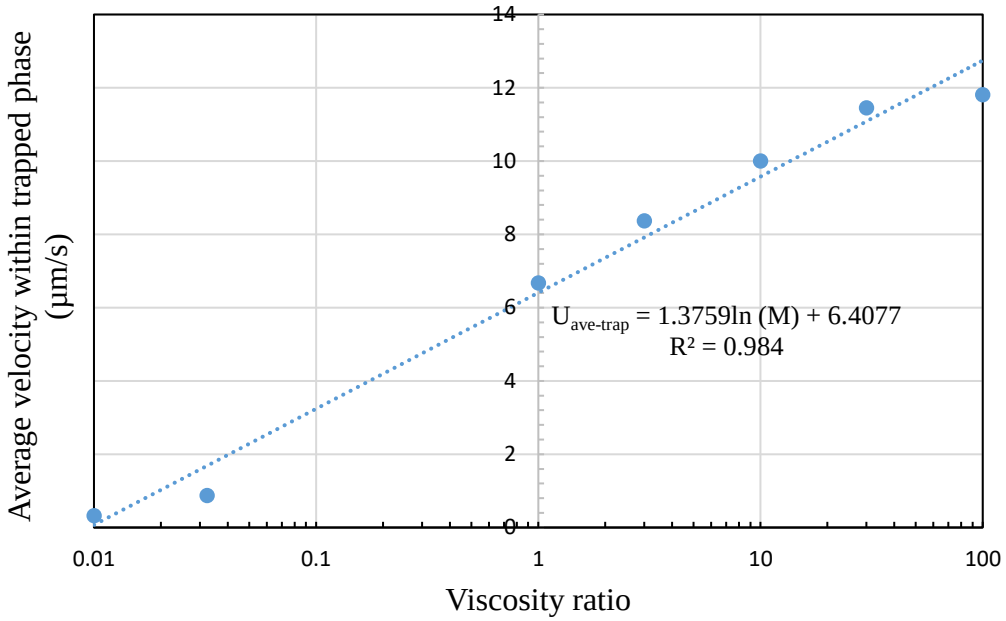

Figure 16 Average velocity of trapped phase versus viscosity ratio

4.4.2. Interfacial Tension (IFT)

As the interfacial tension affects the shape of the liquid/liquid interface (Brackbill et al., 1992), it can directly influence the recirculation of the trapping phase. Therefore, the displacement process from low values for surfactant/hydrocarbon systems to high values for water/hydrocarbon systems is simulated in ranges of 1 to 50 mN/m during an imbibition displacement through the pore-doublet model where the non-wetting phase is patched only on the right-hand cavity. The constant injection velocity is equal to 1×10^{-4} m/s and viscosities are 0.01 and 0.001 Pa.s for invading and trapped phase respectively. As the interfacial tension decreases, the curvature of interface changes from a concave shape to a flatter form; consequently, the centroid of recirculation shifts toward the right side of the pore assembly that can be seen in Figure 17. As the interfacial tension increases, the capillary forces are strengthened; as a result, resistance to flow appears which leads to weakened circulation. Therefore, as it is shown in Figure 18 an overall logarithmic decrease is seen in the average velocity trend as the interfacial tension increases. Changes in interfacial tension reshape the

interface between the invading and trapped phases; consequently, the distribution of drag force along the interface is varied. On the other hand, changes in the location of the centroids in conjugation with changes in drag force distribution cause the logarithmic (non-linear) behavior of average velocity inside the trapped phase.

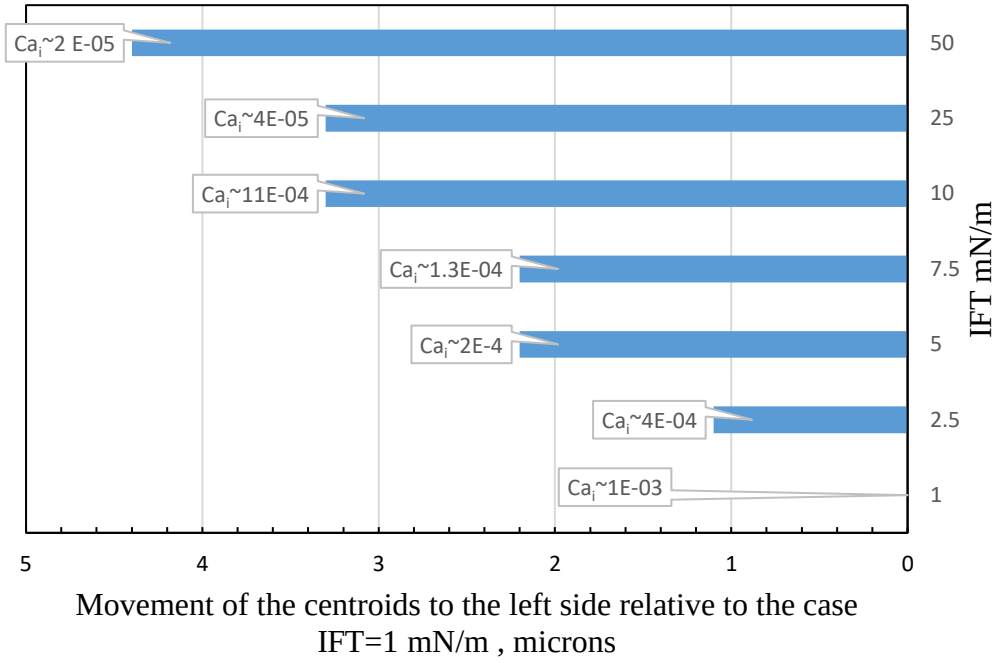

Figure 17 Changes in the location of centroids for different interfacial tension

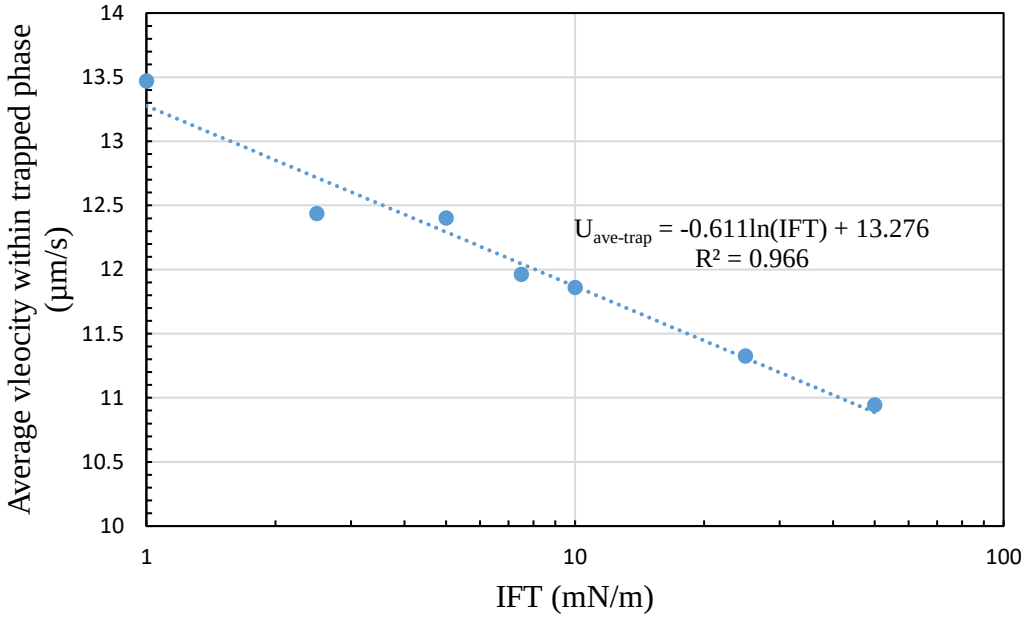

Figure 18 Average velocity of trapped phase versus viscosity ratio

4.4.3. Injection Velocity

To examine the effect of injection velocities on the velocity field through the trapping phase, various injection velocities from 1×10^{-3} to 3×10^{-6} with a stepwise increase for imbibition mechanism were considered. Surface tension is equal to 0.05 N/m and viscosities are 0.01 and 0.001 Pa.s for invading and trapped phase respectively. The results illustrated while the increase in velocity field is linearly proportional to the injection velocity can be seen, no change in location of the centroid is observable. Figure 19 depicts the log-log plot of average velocity inside the trapped phase versus the injected velocity. Linear behavior between the average velocity inside the trapped phase and injection velocity can be seen.

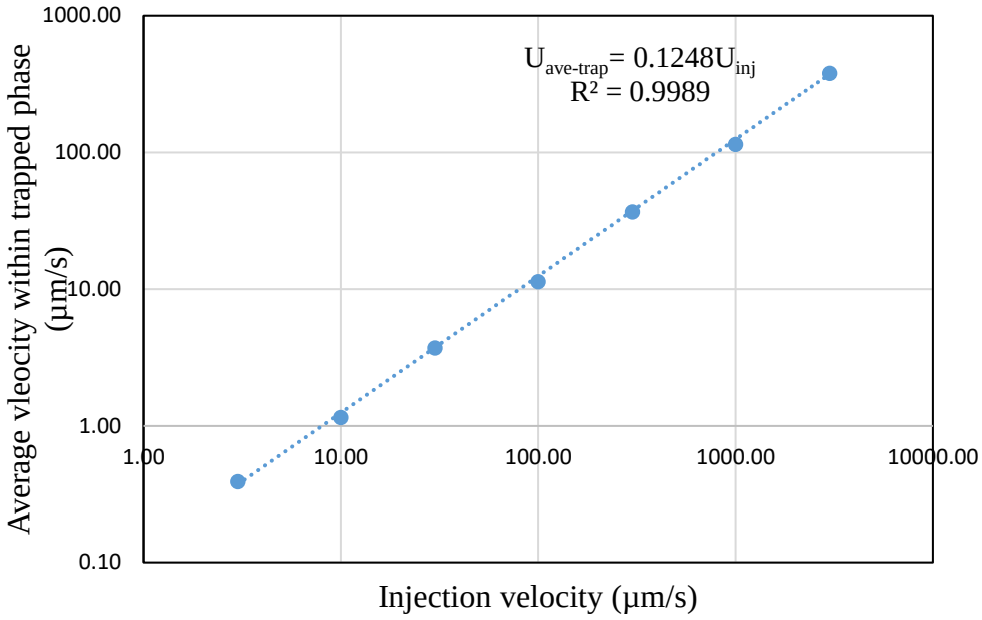

Figure 19 Average velocity of trapped phase versus injection velocity

4.4.4. The Role of Capillary Number

As discussed, displacement mechanism and fluid configurations can influence recirculation behavior inside the trapped phase. Drag force analysis was performed to quantify the recirculation phenomenon. We have shown that how the dynamic parameters are incorporated in capillary number influences recirculation behavior, including average velocity in the trapped phase and centroid movement. Further analysis is required to address the behavior of recirculation phenomenon in response to the changes in capillary number, as a dimensionless number unifying all of these elements. In this regard, the behavior of capillary number of trapped phase ($Ca_t = \frac{U_t \mu_t}{\sigma}$) as a function of capillary number of invading phase for various viscosity ratios is evaluated. As it is shown in Figure 20, a linear relationship between the capillary numbers of trapped and invading phases was found, for all viscosity ratios. For the viscosity ratios more than unity (M>1), increase in viscosity of invading phase results in less capillary number in trapped phase as the less drag force is transmitted to the interface. On the other hand, for the viscosity ratios less than unity (M<1), the amount of drag force transmitted to the fluid-fluid interface is constant and increase in viscosity of trapped phase results in a

minor increase in capillary number of trapped phase. This is attributed to the fact that the effect of increase in viscosity of trapped phase on the capillary number is cancelled out with intensified energy dissipation inside the trapped phase.

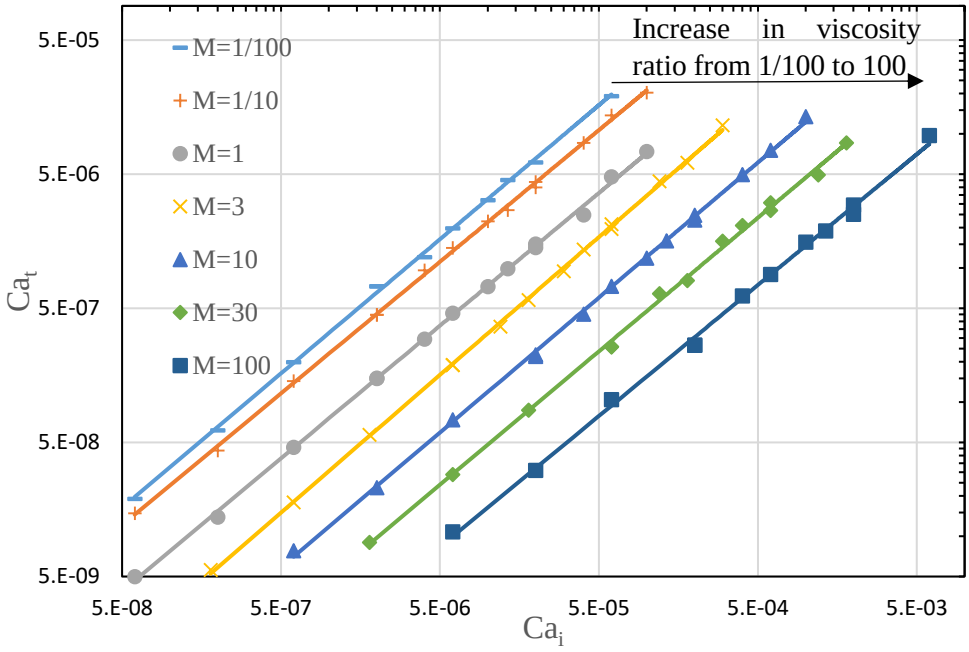

Figure 20 Capillary number of trapped phase as a function of the capillary number of invading phase for various viscosity ratios from 1/00 to 100 (the solid lines are the fitting lines)

Summary and Conclusion

The numerical simulation of the immiscible displacement process through a pore-doublet model was performed in such a way to set trapped-phase patches in specified locations of the pore assembly. To capture the pore-scale processes at low capillary number we used a filtered surface formulation of direct pore-scale modeling for drainage and imbibition mechanisms.

- The results showed, in the case of ranges capillary number of invading phase analyzed in this study (in order of 1×10^{-2} to 1×10^{-7}), that a recirculation phenomenon exists in the

trapped phase, while various behaviors were observed. Zero-velocity zones were observed at the centroids of the recirculation trapped phase.

- In the imbibition mechanism, the convexity of the trapped phase created two stagnant regions in the vicinity of the interface inside the invading fluid. In the drainage mechanism, the concavity of the trapped phase wiped out the stagnant zones inside the invading fluid adjacent to the fluid-fluid interface.
- Drag-force analysis on the liquid-liquid interface shows that the maximum force was exerted near the center of the interface during imbibition, whereas during drainage the greater force was applied on two elongated interface tails on the solid surface. The elongation factor of the centroid is a function of displacement mechanism (Drag-force distribution along the interface), elongated parallel to the interface during drainage, perpendicularly during imbibition.
- The existence of a solid surface accentuated the recirculation process so that one or more centroids can be created, depending on the displacement mechanism. Analysis of drag-force distribution on the solid surface showed that near the centroids adjacent to the solid surface, stagnant zones were created.
- In the case of the lower ratio of the trapped phase's radius to the cavity depth, two simultaneous recirculation zones inside the adjacent invading and trapped phases were formed.
- Fluid dynamic properties play a pivotal role in recirculation behavior: for all viscosity ratios a linear relationship between the capillary numbers of trapped and invading phases exists.
- The combined effects of changes in the drag-force distribution along with the interface of two-phases as well movement of centroids cause logarithmic behavior of average

velocity inside the trapped phase, while this parameter shows a linear trend with changes in injection velocity as the centroid is fixed for various injection velocity.

- These results can be considered as a cornerstone for more complicated cases like CO_2 sequestration or reservoir in situ combustion, where the other parameters can be combined with momentum transfer such as mass and heat transfer. Our quantified recirculation results provide great insights into the mobilization process in porous media where forces such as viscosity, inertia, and capillary forces are working simultaneously.

Acknowledgments

We gratefully acknowledge the financial support provided to the PIVOTS project by the "Région Centre – Val de Loire" and the European Regional Development Fund.

References

Aminnaji, M., Rabbani, A., J. Niasar, V., Babaei, M., 2019. Effects of pore-scale heterogeneity on macroscopic NAPL dissolution efficiency: A two-scale numerical simulation study. Water Resour. Res. 55(11), 8779-8799. https://doi.org/10.1029/2019WR026035

Avraam, D.G., Payatakes, A.C., 1995. Flow regimes and relative permeabilities during steady-state two-phase flow in porous media. J. Fluid Mech. 293, 207–236. https://doi.org/10.1017/S0022112095001698

Batchelor, C.K., Batchelor, G.K., 2000. An introduction to fluid dynamics. Cambridge university press. Cambridge, United Kingdom. https://doi.org/10.1017/CBO9780511800955

Bhaga, D., Weber, M.E., 1981. Bubbles in viscous liquids: shapes, wakes and velocities. J. Fluid Mech. 105, 61–85. https://doi.org/10.1017/S002211208100311X

Blunt, M.J., 2001. Flow in porous media—pore-network models and multiphase flow. Curr. Opin. Colloid Interface Sci. 6(3), 197–207. https://doi.org/10.1016/S1359-0294(01)00084-X

Brackbill, J.U., Kothe, D.B., Zemach, C., 1992. A continuum method for modeling surface tension. J. Comput. Phys. 100(2), 335–354. https://doi.org/10.1016/0021-9991(92)90240-Y

Chatzis, I., Dullien, F.A.L., 1983. Dynamic immiscible displacement mechanisms in pore doublets: theory versus experiment. J. Colloid Interface Sci. 91(1), 199–222. https://doi.org/10.1016/0021-9797(83)90326-0

Dejam, M., Hassanzadeh, H., 2018. Diffusive leakage of brine from aquifers during CO2 geological storage. Adv. Water Resour. 111, 36–57. https://doi.org/10.1016/j.advwatres.2017.10.029

Dejam, M., Hassanzadeh, H., Chen, Z., 2014. Reinfiltration through liquid bridges formed between two matrix blocks in fractured rocks. J. Hydrol. 519, 3520–3530. https://doi.org/10.1016/j.jhydrol.2014.10.050

Ebigbo, A., Golfier, F., Quintard, M., 2013. A coupled, pore-scale model for methanogenic microbial activity in underground hydrogen storage. Adv. Water Resour. 61, 74–85. https://doi.org/10.1016/j.advwatres.2013.09.004

Fakhari, A., Li, Y., Bolster, D., Christensen, K.T., 2018. A phase-field lattice Boltzmann model for simulating multiphase flows in porous media: Application and comparison to experiments of CO2 sequestration at pore scale. Adv. Water Resour. 114, 119–134. https://doi.org/10.1016/j.advwatres.2018.02.005

Ferrari, A., Lunati, I., 2014. Inertial effects during irreversible meniscus reconfiguration in angular pores. Adv. Water Resour. 74, 1–13. https://doi.org/10.1016/j.advwatres.2014.07.009

Ferrari, A., Lunati, I., 2013. Direct numerical simulations of interface dynamics to link capillary pressure and total surface energy. Adv. Water Resour. 57, 19–31. https://doi.org/10.1016/j.advwatres.2013.03.005

Ferziger, J.H., Perić, M., 2002. Computational Methods for Fluid Dynamics, Springer-Verlag Berlin Heidelberg. https://doi.org/10.1007/978-3-642-56026-2

Francois, M.M., Cummins, S.J., Dendy, E.D., Kothe, D.B., Sicilian, J.M., Williams, M.W., 2006. A balanced-force algorithm for continuous and sharp interfacial surface tension models within a volume tracking framework. J. Comput. Phys. 213(1), 141–173. https://doi.org/10.1016/j.jcp.2005.08.004

Gueyffier, D., Li, J., Nadim, A., Scardovelli, R., Zaleski, S., 1999. Volume-of-fluid interface tracking with smoothed surface stress methods for three-dimensional flows. J. Comput. Phys. 152(2), 423–456. https://doi.org/10.1006/jcph.1998.6168

Heshmati, M., Piri, M., 2018. Interfacial boundary conditions and residual trapping: A pore-scale investigation of the effects of wetting phase flow rate and viscosity using micro-particle image velocimetry. Fuel 224, 560–578. https://doi.org/10.1016/j.fuel.2018.03.010

Hirschler, M., Kunz, P., Huber, M., Hahn, F., Nieken, U., 2016. Open boundary conditions for ISPH and their application to micro-flow. J. Comput. Phys. 307, 614–633. https://doi.org/10.1016/j.jcp.2015.12.024

Issa, R.I., 1986. Solution of the implicitly discretised fluid flow equations by operator-splitting. J. Comput. Phys. 62(1) , 40–65. https://doi.org/10.1016/0021-9991(86)90099-9

Jiménez-Martínez, J., Le Borgne, T., Tabuteau, H., Méheust, Y., 2017. Impact of saturation on dispersion and mixing in porous media: Photobleaching pulse injection experiments and shear-enhanced mixing model. Water Resour. Res. 53(2), 1457–1472. https://doi.org/10.1002/2016WR019849

Kang, Q., Zhang, D., Chen, S., 2002. Unified lattice Boltzmann method for flow in multiscale porous media. Phys. Rev. E 66(5), 56307. https://doi.org/10.1103/PhysRevE.66.056307

Kashid, M.N., Gerlach, I., Goetz, S., Franzke, J., Acker, J.F., Platte, F., Agar, D.W., Turek, S., 2005. Internal circulation within the liquid slugs of a liquid− liquid slug-flow capillary microreactor. Ind. Eng. Chem. Res. 44(14), 5003–5010. https://doi.org/10.1021/ie0490536

Kashid, M.N., Harshe, Y.M., Agar, D.W., 2007. Liquid− liquid slug flow in a capillary: an alternative to suspended drop or film contactors. Ind. Eng. Chem. Res. 46(25), 8420–8430. https://doi.org/10.1021/ie070077x

Kazemifar, F., Blois, G., Kyritsis, D.C., Christensen, K.T., 2016. Quantifying the flow dynamics of supercritical CO2–water displacement in a 2D porous micromodel using fluorescent microscopy and microscopic PIV. Adv. Water Resour. 95, 352–368. https://doi.org/10.1016/j.advwatres.2015.05.011

Li, R., Zhang, J., Yong, Y., Wang, Y., Yang, C., 2015. Numerical simulation of steady flow past a liquid sphere immersed in simple shear flow at low and moderate Re. Chinese J. Chem. Eng. 23(1), 15–21. https://doi.org/10.1016/j.cjche.2014.10.005

Li, Y., Kazemifar, F., Blois, G., Christensen, K.T., 2017. Micro-PIV measurements of multiphase flow of water and liquid CO2 in 2-D heterogeneous porous micromodels. Water Resour. Res. 53(7), 6178–6196. https://doi.org/10.1002/2017WR020850

Liu, Z., Zhang, L., Pang, Y., Wang, X., Li, M., 2017. Micro-PIV investigation of the internal flow transitions inside droplets traveling in a rectangular microchannel. Microfluid. Nanofluidics 21(12), 180. https://doi.org/10.1007/s10404-017-2019-z

Ma, S., Sherwood, J.M., Huck, W.T.S., Balabani, S., 2014. On the flow topology inside droplets moving in rectangular microchannels. Lab Chip 14(18), 3611–3620. https://doi.org/10.1039/C4LC00671B

Maes, J., Soulaine, C., 2018. A new compressive scheme to simulate species transfer across fluid interfaces using the volume-of-fluid method. Chem. Eng. Sci. 190, 405–418. https://doi.org/10.1016/j.ces.2018.06.026

Mashayekhizadeh, V., Ghazanfari, M.H., Kharrat, R., Dejam, M., 2011. Pore-level observation of free gravity drainage of oil in fractured porous media. Transp. porous media 87, 561–584. https://doi.org/10.1007/s11242-010-9701-x

Maxworthy, T., Gnann, C., Kürten, M., Durst, F., 1996. Experiments on the rise of air bubbles in clean viscous liquids. J. Fluid Mech. 321, 421–441. https://doi.org/10.1017/S0022112096007781

Meakin, P., Tartakovsky, A.M., 2009. Modeling and simulation of pore-scale multiphase fluid flow and reactive transport in fractured and porous media. Rev. Geophys. 47(3). https://doi.org/10.1029/2008RG000263

Méheust, Y., Løvoll, G., Måløy, K.J., Schmittbuhl, J., 2002. Interface scaling in a two-dimensional porous medium under combined viscous, gravity, and capillary effects. Phys. Rev. E 66(5), 51603. https://doi.org/10.1103/PhysRevE.66.051603

Olayiwola, S.O., Dejam, M., 2019. A comprehensive review on interaction of nanoparticles with low salinity water and surfactant for enhanced oil recovery in sandstone and carbonate reservoirs. Fuel 241, 1045–1057. https://doi.org/10.1016/j.fuel.2018.12.122

Oren, P.-E., Bakke, S., Arntzen, O.J., 1998. Extending predictive capabilities to network models. SPE J. 3(4), 324–336. https://doi.org/10.2118/52052-PA

Pavuluri, S., Maes, J., Doster, F., 2018. Spontaneous imbibition in a microchannel: Analytical solution and assessment of volume of fluid formulations. Microfluid. Nanofluidics 22(8), 90. https://doi.org/10.1007/s10404-018-2106-9

Pilotti, M., Succi, S., Menduni, G., 2002. Energy dissipation and permeability in porous media. EPL (Europhysics Lett). 60(1), 72. https://doi.org/10.1209/epl/i2002-00320-5

Raeini, A.Q., Bijeljic, B., Blunt, M.J., 2014. Numerical modelling of sub-pore scale events in two-phase flow through porous media. Transp. porous media 101(2), 191–213. https://doi.org/10.1007/s11242-013-0239-6

Raeini, A.Q., Blunt, M.J., Bijeljic, B., 2012. Modelling two-phase flow in porous media at the pore scale using the volume-of-fluid method. J. Comput. Phys. 231(17), 5653–5668. https://doi.org/10.1016/j.jcp.2012.04.011

Riazi, M., Sohrabi, M., Bernstone, C., Jamiolahmady, M., Ireland, S., 2011. Visualisation of mechanisms involved in CO2 injection and storage in hydrocarbon reservoirs and water-

bearing aquifers. Chem. Eng. Res. Des. 89(9), 1827–1840. https://doi.org/10.1016/j.cherd.2011.03.009

Roman, S., Soulaine, C., AlSaud, M.A., Kovscek, A., Tchelepi, H., 2016. Particle velocimetry analysis of immiscible two-phase flow in micromodels. Adv. Water Resour. 95, 199–211. https://doi.org/10.1016/j.advwatres.2015.08.015

Roman, S., Soulaine, C., Kovscek, A.R., 2019. Pore-scale visualization and characterization of viscous dissipation in porous media. J. Colloid Interface Sci. 558, 269-279. https://doi.org/10.1016/j.jcis.2019.09.072

Sarrazin, F., Loubiere, K., Prat, L., Gourdon, C., Bonometti, T., Magnaudet, J., 2006. Experimental and numerical study of droplets hydrodynamics in microchannels. AIChE J. 52(12), 4061–4070. https://doi.org/10.1002/aic.11033

Shams, M., Raeini, A.Q., Blunt, M.J., Bijeljic, B., 2018. A study to investigate viscous coupling effects on the hydraulic conductance of fluid layers in two-phase flow at the pore level. J. Colloid Interface Sci. 522, 299–310. https://doi.org/10.1016/j.jcis.2018.03.028

Weller, H.G., Tabor, G., Jasak, H., Fureby, C., 1998. A tensorial approach to computational continuum mechanics using object-oriented techniques. Comput. Phys. 12(6), 620–631. https://doi.org/10.1063/1.168744

Yang, G., Chu, X., Vaikuntanathan, V., Wang, S., Wu, J., Weigand, B., Terzis, A., 2020. Droplet mobilization at the walls of a microfluidic channel. Phys. Fluids 32 (1), 12004. https://doi.org/10.1063/1.5139308

Yang, G., Terzis, A., Zarikos, I., Hassanizadeh, S.M., Weigand, B., Helmig, R., 2019. Internal flow patterns of a droplet pinned to the hydrophobic surfaces of a confined microchannel using micro-PIV and VOF simulations. Chem. Eng. J. 370, 444–454. https://doi.org/10.1016/j.cej.2019.03.191

Zarikos, I., Terzis, A., Hassanizadeh, S.M., Weigand, B., 2018. Velocity distributions in trapped and mobilized non-wetting phase ganglia in porous media. Sci. Rep. 8(1), 13228. https://doi.org/10.1038/s41598-018-31639-4

Zhao, X., Blunt, M.J., Yao, J., 2010. Pore-scale modeling: Effects of wettability on waterflood oil recovery. J. Pet. Sci. Eng. 71(3-4), 169–178. https://doi.org/10.1016/j.petrol.2010.01.011

Appendix A

ρ and μ, respectively density and viscosity of the VOF mixture, are calculated using the indicator function $\alpha \in [0, 1]$ representing the volume fraction of one of the phases in a controlled volume:

$$\rho = \alpha\rho_w + (1-\alpha)\rho_{nw} \quad \text{A-1}$$

$$\mu = \alpha\mu_w + (1-\alpha)\mu_{nw} \quad \text{A-2}$$

where the indices w and nw denote wetting and non-wetting fluids respectively.

Inaccurate representation of capillary forces results in smeared color function. Raeini et al (2012) suggested a sharpening color function to solve this problem. Using Sharp Surface Force modeling (SSF) approach, capillary body forces based on Equation 6 are given by,

$$\boldsymbol{f}_{c,SSF} = \sigma\nabla.\left(\frac{\boldsymbol{\nabla}\alpha_s}{|\boldsymbol{\nabla}\alpha_s|}\right)\boldsymbol{\nabla}\alpha_{shp} \quad \text{A-3}$$

where the smoothed color function is given by,

$$\alpha_s = \langle\langle\alpha\rangle_{center\to face}\rangle_{face\to center} \quad \text{A-4}$$

where the indices center and face denote the cell center and face center respectively. Also, the modified sharpened color function is given by (Raeini et al., 2012),

$$\alpha_{shp} = \frac{1}{1-2C_{shp}}\left[\min\left(\max\left(\alpha, C_{shp}\right), 1-C_{shp}\right) - C_{shp}\right] \quad \text{A-5}$$

where $C_{shp} \in [0,0.5)$ denotes the heuristic sharpening coefficient. While $C_{shp} = 0$ results in original CSF formulation, as C_{shp} approaches 0.5 becomes sharper.

Although the SSF formulation can appropriately eliminate the non-physical velocities in the absence of complex solid boundaries, the parasitic currents appear close to curved or edged solid boundaries. To address this issue, capillary-induced flows that results in currents parallel to fluid interfaces are modified as:

$$\boldsymbol{f}_{c,filt} = \boldsymbol{f}_{c,SSF} - \boldsymbol{f}_{c,filt\parallel} \quad \text{A-6}$$

The capillary forces parallel to the interface starts from zero as initial condition and is updated as follows :

$$\boldsymbol{f}_{c,filt\parallel} = \delta_1\left(\boldsymbol{f}^{old}_{c,filt\parallel} + C_{filt\parallel}(\nabla p_c - (\nabla p_c.\boldsymbol{n_I})\boldsymbol{n_I}\right) \quad \text{A-7}$$

where $C_{filt\parallel}$ in Equation A-7 is the filtering coefficient determining the speed of non-physical velocity filtration and is set to 0.1.

δ_1 restricts the correction term to the sharpened interfacial region,

$$\delta_1 = \left|\frac{\nabla\alpha_{shp}}{\nabla\alpha_{shp}+\epsilon}\right| \quad \text{A-8}$$

$\boldsymbol{f}^{old}_{c,filt\parallel}$ denotes the value of $\boldsymbol{f}_{c,filt\parallel}$ at the previous time step, and the term $((\nabla p_c - (\nabla p_c.\boldsymbol{n_I})\boldsymbol{n_I})$ represent the capillary term parallel to the interface.

Appendix B

The figures below show how the velocity is distributed inside the trapped phases for various locations of pore assembly. Also, it shows that the velocity inside the trapped phase is noticeably less than the adjacent invading phase. Closing to the wall solid surface the velocity decreases. The direction of rotation inside the trapped phase is a function of fluid configuration within the pore assembly as well as the direction of flow.

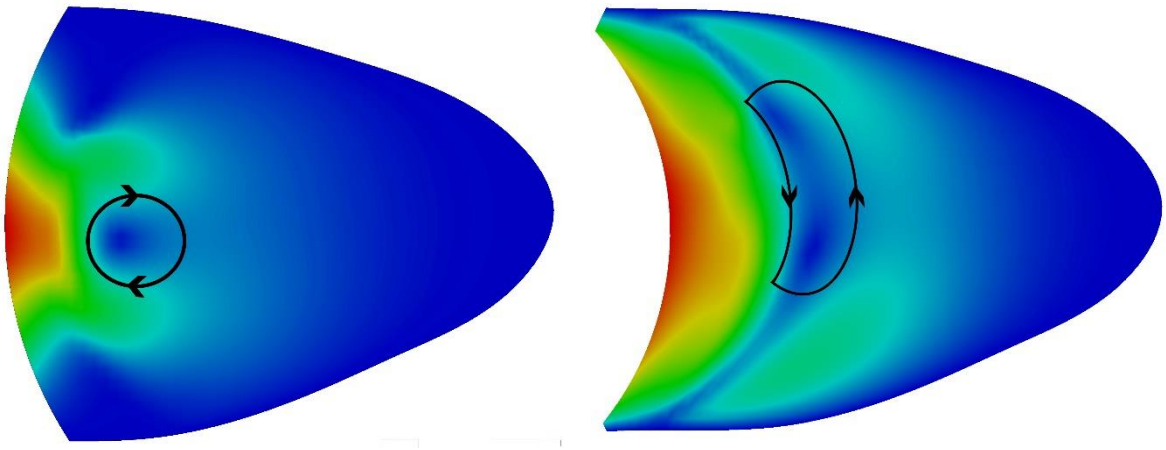

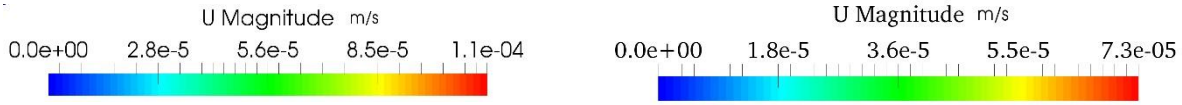

(a) (b)

Figure B1 2D surface plot of velocity on the right side of the pore assembly: (a) Imbibition mechanism, and (b) Drainage mechanism; (the arrows schematically show the rotation around the centroid, and colors show the velocity magnitude, blue color is low velocity zone and red color is high velocity zone).

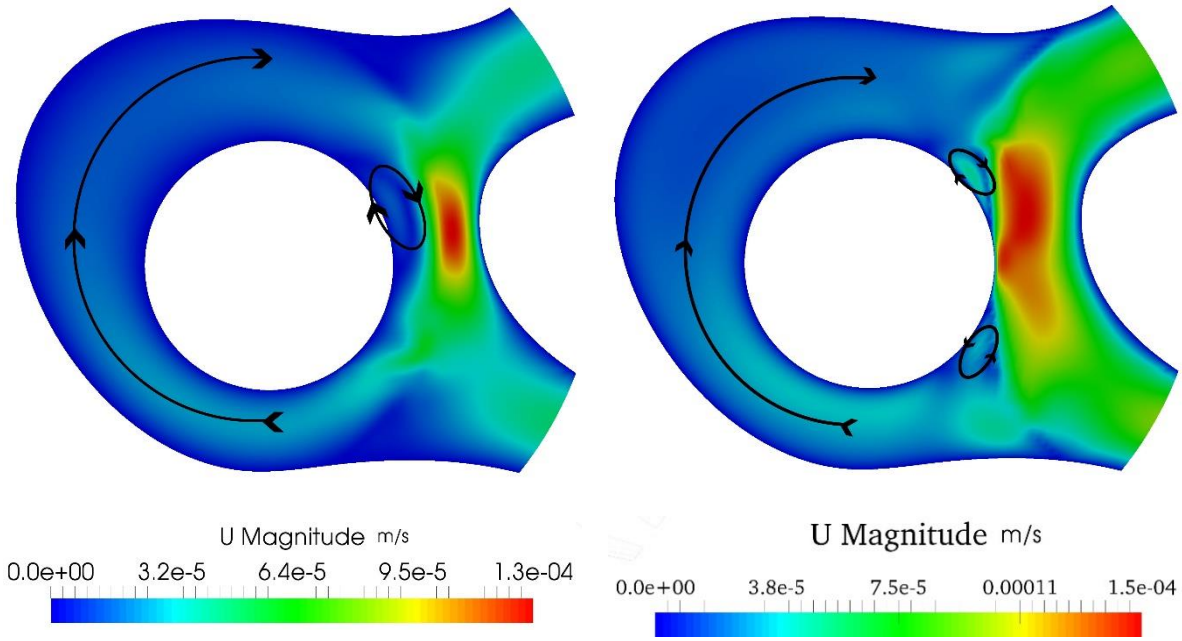

(a) (b)

Figure B2 2D surface plot of velocity on the left side of the pore assembly: (a) Imbibition mechanism and (b) Drainage mechanism; (the arrows schematically show the rotation around the centroid, and colors show the velocity magnitude, blue color is low velocity zone and red color is high velocity zone).

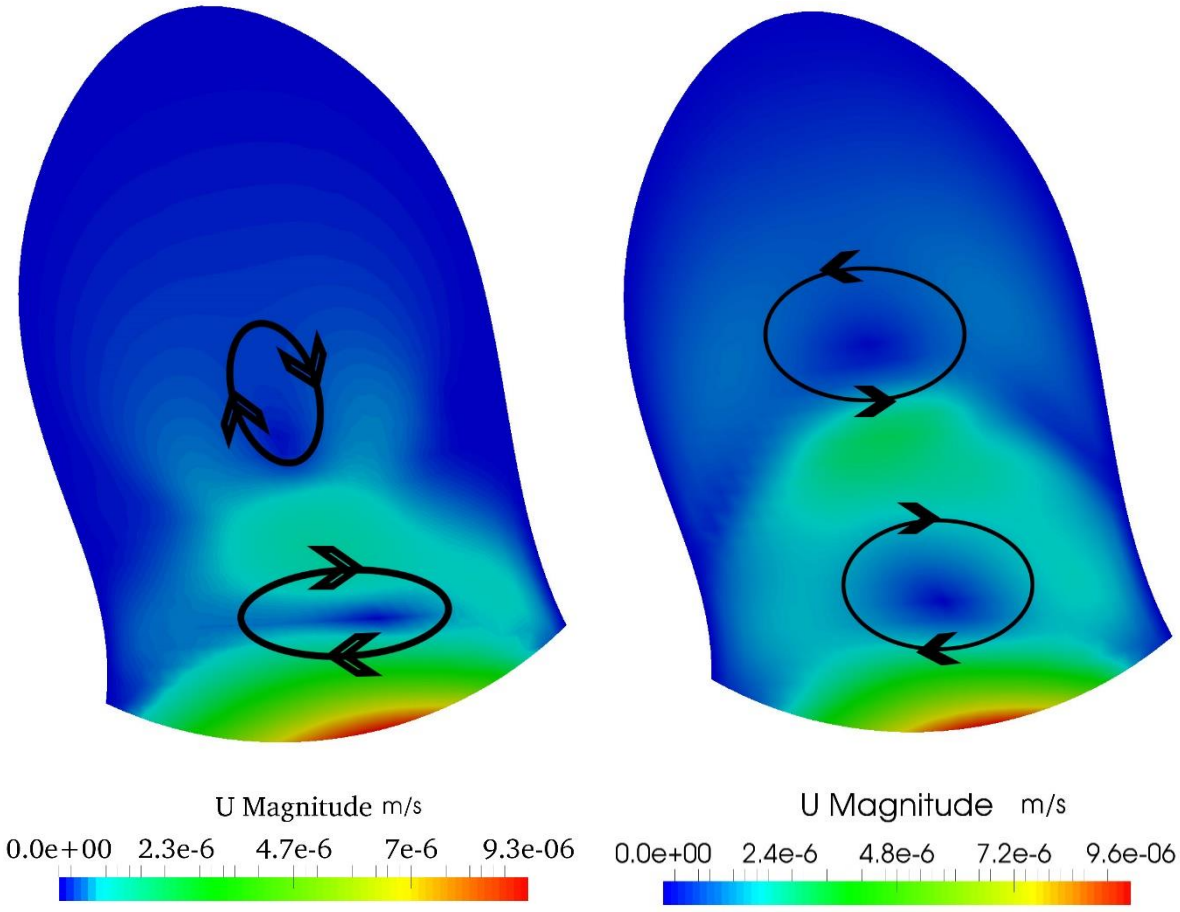

(a) (b)

Figure B3 2D surface plot of velocity on the bottom dead end: (a) Imbibition mechanism, and (b) Drainage mechanism; (the arrows schematically show the rotation around the centroid, and colors show the velocity magnitude, blue color is low velocity zone and red color is high velocity zone).